Nano Research

Open Access

Research Article

An NIR-responsive PDA@RES core-shell nanoplatform accelerates chronic wound healing by remodeling mitochondrial homeostasis and reversing cellular senescence

Jian Feng[1,2], Huixin Lv[3,4], Sicong Ren[5], Yuemeng Zhu[1,2], Yuzhu Han[1,2], Mucong Li[1,2], Jingxia Chen[1,2], Jiaxin Luo[1,2], Dixin He[1,2], Yidi Zhang[1,2] ✉, and Yanmin Zhou[1,2] ✉

[1] *Hospital of Stomatology, Jilin University, Changchun 130021, China*
[2] *Jilin Provincial Key Laboratory of Tooth Development and Bone Remodeling, Changchun 130021, China*
[3] *Department of Prosthodontics, Peking University School and Hospital of Stomatology, Beijing 100081, China*
[4] *National Center for Stomatology and National Clinical Research Center for Oral Diseases and National Engineering Research Center of Oral Biomaterials and Digital Medical Devices and Beijing Key Laboratory of Digital Stomatology and National Health Commission Key Laboratory of Digital Technology of Stomatology, Beijing 100081, China*
[5] *The fourth affiliated hospital, Zhejiang University School of Medicine, Yiwu 322000, China*

Cite this article: *Nano Research*, **2026**, *19*, 94908573. https://doi.org/10.26599/NR.2026.94908573

ABSTRACT: Chronic wound healing remains a significant clinical challenge due to persistent inflammation, oxidative stress, mitochondrial dysfunction, and cellular senescence. A near-infrared (NIR)-responsive polydopamine-resveratrol (PDA@RES) core-shell nanoplatform was developed to address these interconnected pathological mechanisms through synergistic photothermal therapy and drug delivery. The nanoplatform exhibited excellent photothermal conversion capability and demonstrated superior antioxidant and anti-inflammatory effects, effectively scavenging intracellular reactive oxygen species (ROS), restoring mitochondrial membrane potential, and repolarizing macrophages toward a pro-healing phenotype. Mechanistically, the platform activated the AMPK/PGC-1α signaling axis, initiating programmed mitochondrial homeostasis remodeling through enhanced mitophagy and biogenesis, thereby blocking senescence-inducing signals and reversing cellular senescence. The immune microenvironment remodeling subsequently promoted vascular endothelial cell migration and angiogenesis. In diabetic rat models, the NIR-responsive nanoplatform significantly accelerated wound healing by promoting collagen deposition, balancing the immune microenvironment, and facilitating functional vascular regeneration. Notably, the treatment induced nascent hair follicle structures, achieving high-quality regenerative healing rather than scar formation. This study provides an efficient, multi-target synergistic therapeutic strategy for chronic wound healing.

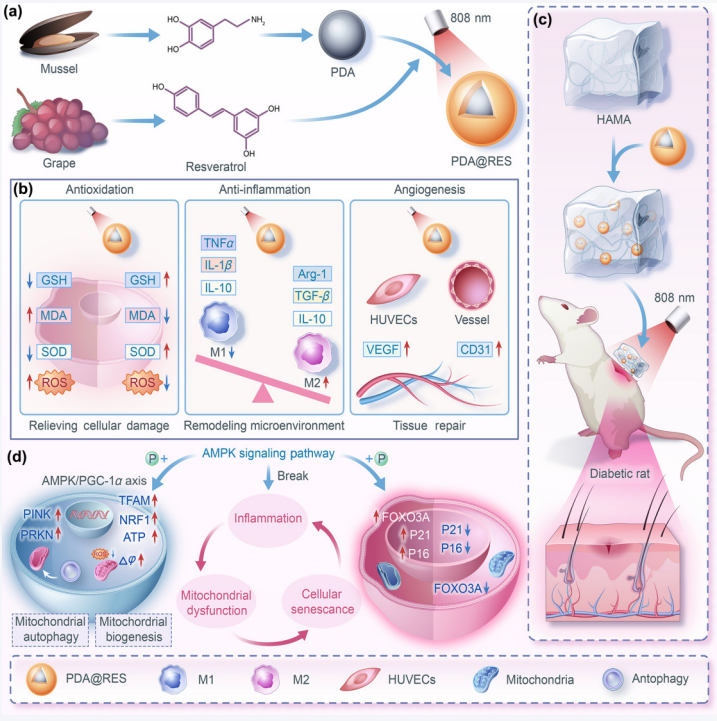

KEYWORDS: chronic wound healing, near-infrared (NIR)-responsive nanoplatform, photothermal synergy, AMPK signaling pathway, mitochondrial homeostasis, cellular senescence

Received: December 14, 2025; **Revised:** February 9, 2026; **Accepted:** February 13, 2026

✉Address correspondence to Yidi Zhang, zhangyidi@jlu.edu.cn; Yanmin Zhou, zhouym@jlu.edu.cn

1 Introduction

Chronic non-healing wounds represent a major global public health challenge, with their complex pathological processes leading to stagnant tissue repair that severely affects patient quality of life and imposes substantial healthcare economic burdens [1, 2]. Under metabolic disease conditions such as diabetes, metabolic disorders and immune dysregulation create a microenvironment with unique pathological characteristics. This microenvironment features persistent inflammatory responses, tissue hypoxia, and excessive accumulation of reactive oxygen species (ROS) [3, 4]. The complex pathological state severely impairs the function of key reparative cells, including fibroblasts and endothelial cells. Consequently, traditional therapeutic strategies, such as advanced dressings and exogenous growth factors, often fail to fundamentally reverse this adverse condition due to their lack of targeting specificity. Therefore, developing novel therapies that target the core pathological mechanisms has become an urgent clinical need [5].

In-depth pathological studies have demonstrated that sustained pathological stress causes critical functional impairment in mitochondria, the cellular energy hub [6]. While this mitochondrial damage affects the entire cellular landscape including both tissue-resident cells and infiltrating immune cells, recent pivotal studies have highlighted the hierarchical role of immune metabolic regulation. Specifically, mitochondrial metabolism in macrophages has been identified as a central checkpoint that dictates the inflammatory rhythm of wound healing. For instance, Willenborg et al. [7] demonstrated that mitochondrial respiration coordinates the stage-specific functions of macrophages, driving the transition from a pro-inflammatory to a pro-resolving phenotype. Similarly, Xu et al. [8] reported that modulating immune metabolism is a powerful strategy to manage dynamic inflammation. These findings indicate that macrophages function as the upstream conductors of the repair process. Although tissue-resident cells such as fibroblasts and endothelial cells are the ultimate executors of structure building, their regenerative function is strictly dependent on a permissive immune microenvironment. When macrophage mitochondrial homeostasis remains disrupted, the resulting persistent inflammatory signals continuously suppress the reparative capacity of downstream tissue cells. Consequently, targeting the mitochondrial homeostasis of macrophages represents a critical upstream therapeutic strategy and a prerequisite for creating a favorable microenvironment for subsequent angiogenesis and tissue remodeling.

As the central nexus for cellular metabolism, signal transduction, and ROS generation, mitochondria become primary targets of attack in the chronic wound microenvironment [9]. Persistent oxidative stress not only causes mitochondrial membrane potential decline and electron transport chain dysfunction but also disrupts mitochondrial dynamics equilibrium. This damage diminishes mitochondrial capacity to scavenge ROS while conversely exacerbating mitochondrial ROS leakage, forming an initial vicious cycle of ROS-mitochondrial damage-ROS re-explosion [10]. The consequences of this damage extend beyond simple functional impairment, triggering a severe imbalance in mitochondrial homeostasis [11, 12]. First, mitochondrial dysfunction leads to sharp reductions in adenosine triphosphate (ATP) generation, severely inhibiting energy-intensive reparative behaviors such as cell proliferation, migration, and tissue remodeling due to energy depletion [13]. Second, the cellular quality control mechanisms for clearing damaged mitochondria (mitophagy) and generating healthy mitochondria (mitochondrial biogenesis) are severely obstructed [14–18]. The continuous accumulation of damaged mitochondria and depletion of healthy mitochondria constitute key driving factors for chronic wound repair stagnation [19]. This mitochondrial homeostasis imbalance directly induces cells to enter a premature senescent state [20–23]. The accumulation of prematurely senescent cells, particularly in inflammatory environments, exhibits persistent pro-inflammatory characteristics, constituting the pathological state of inflammatory senescence. This phenomenon not only exacerbates deterioration of the local microenvironment but also suppresses critical repair events such as vascular regeneration [24–26]. Therefore, breaking this pathological cycle centered on mitochondrial homeostasis collapse represents a key approach to achieving effective repair. While advanced nanotherapies have recently emerged as promising alternatives to traditional treatments [5, 27, 28], a systematic evaluation reveals significant limitations in their therapeutic depth regarding this complex pathology. Most existing antioxidant nanoplatforms primarily focus on the passive scavenging of excessive ROS. Although this approach provides temporary relief, it essentially addresses the symptoms rather than the root cause. These single-target strategies often fail to intervene in the core pathological machinery of mitochondrial homeostasis imbalance, such as obstructed mitophagy and impaired biogenesis. Without restoring mitochondrial quality control, the cleared ROS will rapidly regenerate due to continuous leakage from the damaged electron transport chain. More importantly, few current strategies possess the capability to effectively reverse the established state of cellular senescence. Consequently, there remains a lack of integrated therapeutic strategies capable of simultaneously breaking the vicious ROS cycle, remodeling mitochondrial homeostasis, and rejuvenating senescent executor cells.

Extensive research has demonstrated that adenosine monophosphate (AMP)-activated protein kinase (AMPK) functions as a master regulator of mitochondrial quality control [29–31]. Mechanistically, activated AMPK phosphorylates the downstream effector peroxisome proliferator-activated receptor gamma coactivator 1-alpha (PGC-1α), which drives mitochondrial biogenesis to replenish the healthy mitochondrial pool. Simultaneously, AMPK initiates the clearance of dysfunctional mitochondria known as mitophagy. However, in the specific context of chronic diabetic wounds, the persistent hyperglycemic environment suppresses AMPK signaling. This leads to a dual failure including the inability to clear damaged mitochondria and the stagnation of generating new ones. The consequent accumulation of mitochondrial dysfunction creates a continuous source of oxidative stress which directly induces cellular senescence and the secretion of pro-inflammatory factors. Therefore, scavenging ROS to relieve upstream suppression and effectively reactivating the AMPK signaling axis are crucial for curbing pathological cycles and restoring cellular function.

Resveratrol (RES), a renowned natural polyphenol, serves not only as a potent antioxidant responsible for scavenging ROS and alleviating initial oxidative stress but is also widely reported as a key activator of the AMPK signaling pathway [32–35]. However, its poor solubility, insufficient stability, and lack of controlled release systems severely limit its clinical application. In our previous studies, we demonstrated that resveratrol could form stable and well-dispersed nanospheres through phenol-formaldehyde resin reactions and could encapsulate water-dispersible particles [36]. Near-infrared light-responsive drug delivery platforms have been

employed to improve drug delivery performance. Among these, polydopamine (PDA) nanoparticles possess excellent antioxidant properties, biocompatibility, and photothermal stability, making them recognized as highly efficient photothermal conversion agents (PTAs) [37–39]. These findings suggest that nanoplatforms based on resveratrol and PDA may hold promise for treating refractory wounds by targeting mitochondrial homeostasis.

In this study, we constructed a near-infrared (NIR) responsive core-shell nanoplatform (PDA@RES) (Scheme 1) using PDA as the core and resveratrol (RES) as the shell, aiming to develop a nanoplatform capable of synergistic antioxidant activity, mitochondrial homeostasis remodeling, and angiogenesis promotion. The PDA@RES core-shell structure enables stable loading of RES. We propose the scientific hypothesis that PDA@RES, upon NIR irradiation, can effectively remodel mitochondrial homeostasis through the synergistic action of photothermal effects and RES. The platform can effectively scavenge ROS, restore mitochondrial function, and activate the key AMPK signaling pathway, thereby restoring cellular energy metabolism and homeostatic balance. Ultimately, this approach achieves reversal of cellular senescence, promotion of angiogenesis, and suppression of excessive inflammation to break the pathological vicious cycle of wound healing. To verify this hypothesis, we constructed a diabetic rat skin wound model and systematically validated the biological effects of the platform from *in vitro* to *in vivo*, while conducting in-depth investigation of its molecular mechanisms for regulating mitochondrial homeostasis and reversing cellular senescence.

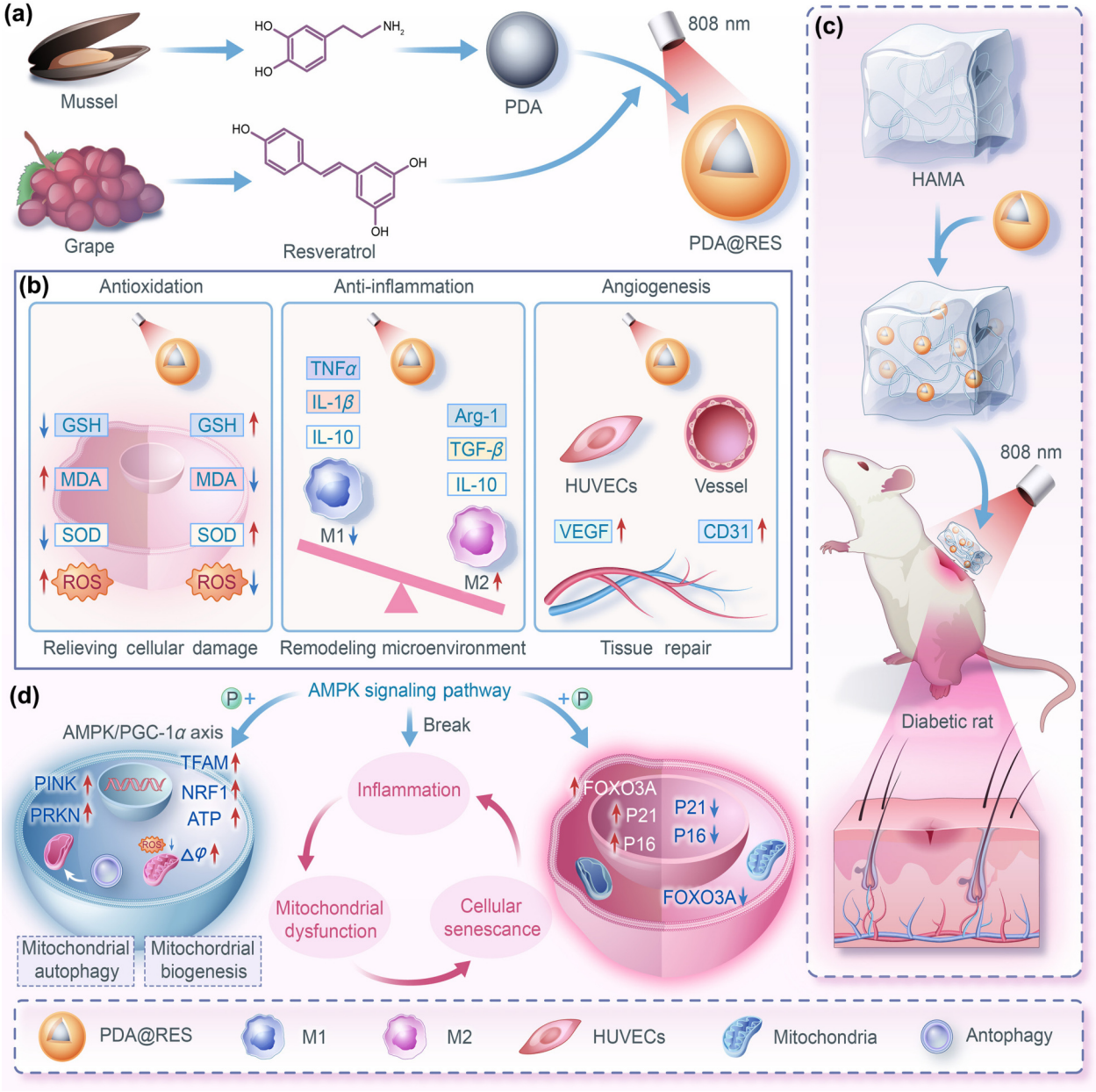

Scheme 1 (a) Synthesis of the near-infrared responsive PDA@RES core-shell nanoplatform. (b) Multiple biological effects of PDA@RES: antioxidant, anti-inflammatory, and pro-angiogenic properties. (c) PDA@RES-loaded hydrogel system for synergistic treatment of diabetic rat skin wounds under NIR irradiation. (d) PDA@RES activates the AMPK signaling pathway, breaking the pathological cycle of inflammation-cellular senescence-mitochondrial dysfunction and promoting healing through reversing senescence and remodeling mitochondrial homeostasis.

2 Results and discussion

2.1 Synthesis and characterization of PDA@RES

The construction of the PDA@RES core-shell nanoplatform was based on an *in situ* crosslinking strategy mediated by electrostatic assembly. As shown in Fig. 1, we first prepared the PDA core through oxidative self-polymerization of dopamine in an alkaline microenvironment. The PDA core exhibited significant negative potential due to deprotonation of surface phenolic hydroxyl groups (Fig. 1(c)). Subsequently, utilizing this electrostatic attraction and π-π stacking interactions, positively charged RES oligomer intermediates were directionally enriched on the PDA surface and solidified *in situ* into a dense polymer shell through phenol-formaldehyde polycondensation reactions. Zeta potential analysis (Fig. 1(c)) confirmed that the surface charge of the nanoparticles underwent significant reversal after coating, which strongly demonstrated that the negatively charged core had been effectively shielded and encapsulated by the RES shell. Transmission electron microscopy (TEM) images intuitively confirmed this structure. The PDA core appeared as morphologically uniform, electron-dense solid nanospheres (Fig. 1(a)), while PDA@RES clearly displayed a lighter-colored polymer shell coating around the dark PDA core (Fig. 1(b)). Dynamic light scattering (DLS) measurements also corroborated shell formation, with the average hydrodynamic diameter of nanoparticles increasing from approximately 139.9 nm for PDA (Fig. 1(d)) to approximately 256.2 nm for PDA@RES (Fig. 1(e)).

The chemical composition of this core-shell structure was further confirmed by a series of spectroscopic characterizations. Ultraviolet–visible (UV–vis) spectroscopy (Fig. 1(f)) showed that the PDA@RES spectrum successfully superimposed the characteristics of both components. It not only retained the broad-spectrum absorption properties of the PDA core from the visible to near-infrared region but also displayed the characteristic absorption peak of RES near 300 nm. X-ray photoelectron spectroscopy (XPS) analysis (Figs. 1(g)–1(i), and Fig. S1 in the Electronic Supplementary Material (ESM)) provided more critical surface evidence. High-resolution C 1s spectra (Fig. 1(h)) revealed that compared to PDA, PDA@RES showed relatively increased peak intensity at the C–O position, attributed to the abundant phenolic hydroxyl structures in the RES shell. Most critically, N 1s spectra (Fig. 1(i)) showed that the C-N bond signal originating from the PDA core was significantly weakened in PDA@RES, strongly indicating that the PDA core had been successfully encapsulated by the RES shell. Fourier transform infrared spectroscopy (FTIR) (Fig. 1(j)) further provided evidence at the functional group level. The PDA@RES spectrum integrated the characteristic peaks of both PDA and RES, indicating that RES had been successfully loaded onto PDA. Finally, thermogravimetric analysis (TGA) (Fig. 1(k), and Fig. S2 in the ESM) further confirmed the loading by evaluating thermal stability. TGA curves showed that upon heating to 800 °C, the mass losses of pure PDA, RES, and PDA@RES were approximately 55.69%, 47.58%, and 49.39%, respectively. The thermal weight loss characteristics of PDA@RES fell between those of the two raw materials, which conforms to the characteristics of composite materials and further confirms the successful loading of RES. To further quantify the drug loading capacity, the loading efficiency was assessed via UV–vis spectrophotometry. The PDA@RES nanoplatform yielded a high encapsulation efficiency (EE) of 99.2% and a drug loading content (DLC) of 68.9%, indicating the superior payload capability of the core-shell architecture. Furthermore, the *in vitro* release profiles were investigated under different conditions (Fig. S3 in the ESM). In a neutral environment (pH 7.4), the nanoplatform exhibited a relatively slow and sustained release profile. In contrast, the release rate increased significantly under acidic conditions (pH 5.5), which is favorable for targeting the acidic microenvironment of chronic wounds. Notably, a burst release of RES was triggered upon NIR irradiation, attributed to the photothermal effect of the PDA core disrupting the drug-carrier interaction. This pH/NIR-dual responsive behavior ensures precise, on-demand delivery of RES to the lesion site. This precise core-shell structural design aims to overcome the inherent defects of natural resveratrol, including poor water solubility and a tendency to aggregate, while optimizing the surface-to-volume ratio to reduce the total RES dosage and avoid potential cytotoxicity. More importantly, this spatial close coupling retains the photothermal conversion capability of the PDA core, laying an ideal physical foundation for achieving NIR-triggered efficient photothermal-drug synergistic therapy.

To systematically verify the photothermal conversion performance of this nanoplatform, we conducted comprehensive detection of its potential photothermal properties. Theoretically, the catechol structure of PDA enables it to effectively absorb NIR photon energy and release it in the form of thermal energy, providing an ideal physical foundation for NIR-responsive synergistic therapy. When exposed to 808 nm NIR light (1.5 W/cm^2) irradiation, as shown in Figs. 2(a) and 2(b), the temperature of the PBS control group showed almost no change. In contrast, both PDA NPs and PDA@RES NPs induced significant temperature increases, indicating that the photothermal conversion capability of this nanoplatform indeed originates from its PDA core. Notably, the temperature of PDA@RES NPs rapidly increased from 26.0 to 41.6 °C within 6 min. This temperature is crucial for photothermal responsive nanomaterials to exert biological effects *in vivo*. Unlike intense photothermal therapy that may cause thermal damage to surrounding normal tissues, this mild photothermal temperature not only meets the needs of promoting local circulation and activating cellular metabolism but also maximally avoids side effects such as thermal injury [40–42]. Additionally, the continuous temperature changes of the nanoparticle solution, including both the heating and natural cooling processes, were recorded (Fig. 2(c)). Furthermore, we explored the controllability of this photothermal effect. As the concentration of PDA@RES NPs increased from 0 to 200 μg/mL, the maximum temperature of the solution increased after 5 min of NIR irradiation at 1.5 W/cm^2 (Fig. 2(d)), indicating that the photothermal conversion of PDA@RES NPs exhibits concentration dependence. Meanwhile, its photothermal performance also demonstrates intensity dependence. As shown in Fig. 2(e), at a fixed concentration, when the NIR light intensity increased from 0.5 to 2.0 W/cm^2, the solution temperature increased accordingly. This concentration and intensity-dependent photothermal conversion mode makes this nanoplatform more precisely controllable in future biomedical applications [43]. Finally, the photothermal repeatability of PDA@RES NPs was detected by switching the 808 nm NIR laser on and off. As shown in Fig. 2(f), after five heating and cooling cycles, the maximum temperature of PDA@RES NPs showed no significant attenuation. This indicates that PDA@RES NPs exhibit excellent recycling stability in terms of their light absorption

capacity and photothermal conversion characteristics. To further quantify the photothermal capability, the photothermal conversion

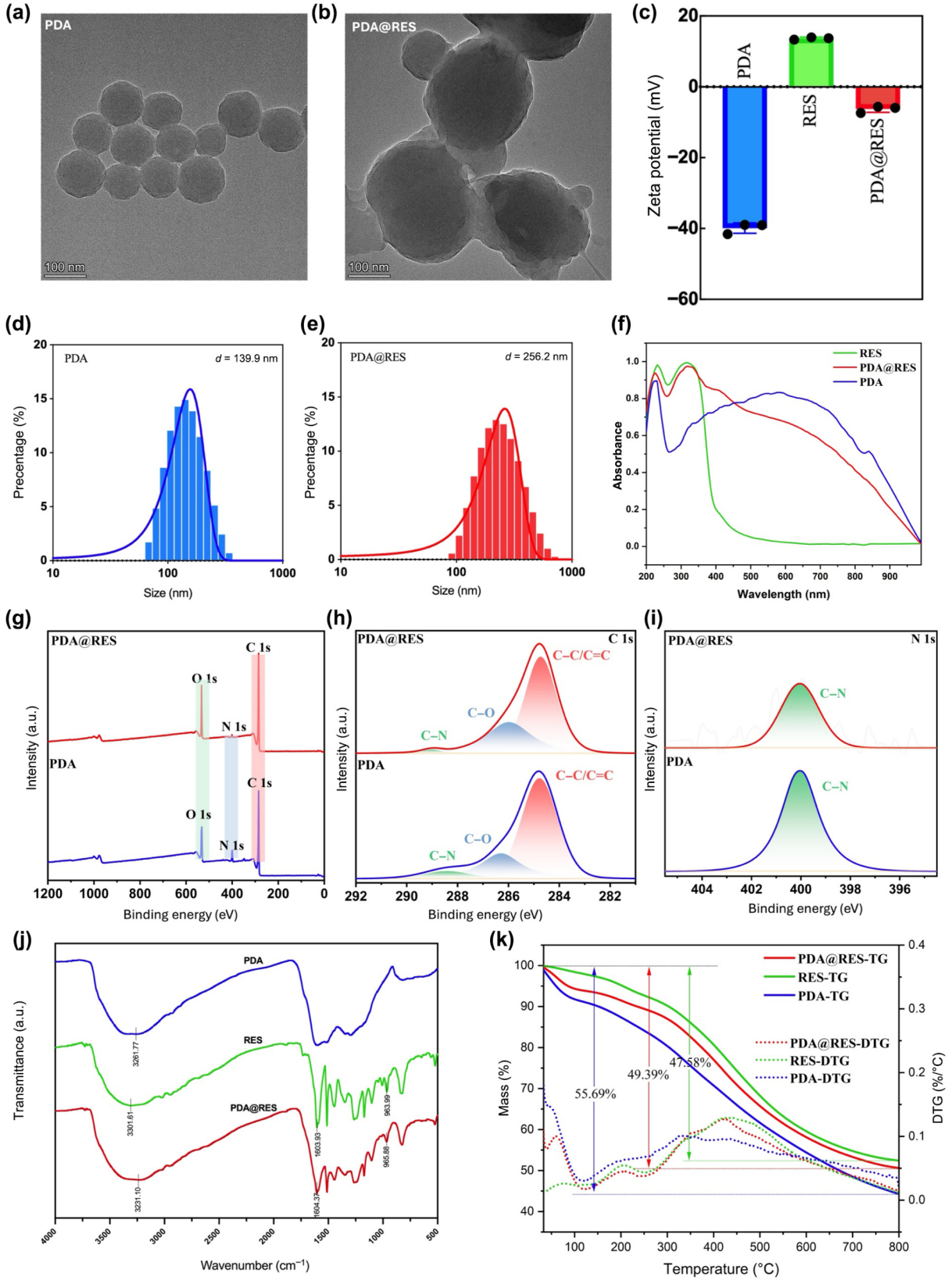

Figure 1 Preparation and characterization of near-infrared light-responsive PDA@RES NPs. TEM images of (a) PDA NPs and (b) PDA@RES NPs. (c) Zeta potential of PDA NPs, RES NPs, and PDA@RES NPs. Diameter of (d) PDA NPs and (e) PDA@RES NPs. (f) UV–vis spectra of PDA NPs, RES NPs, and PDA@RES NPs. (g) XPS spectra of PDA NPs and PDA@RES NPs. High-resolution spectra of (h) C 1s and (i) N 1s for PDA NPs and PDA@RES NPs. (j) Fourier transform infrared spectra of PDA NPs, RES NPs, and PDA@RES NPs. (k) Thermogravimetric analysis (TG-DTG) of PDA NPs, RES NPs, and PDA@RES NPs.

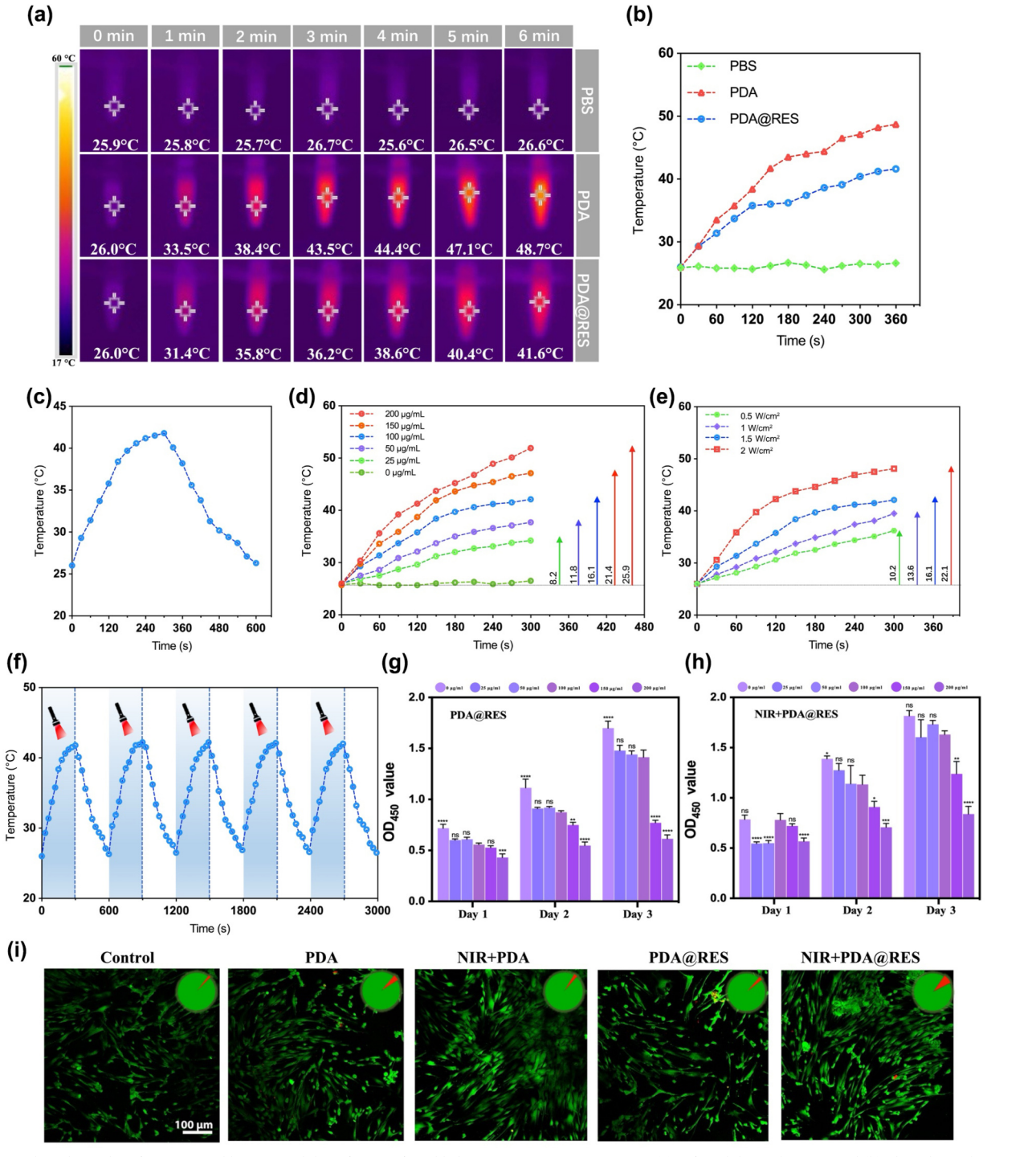

Figure 2 Photothermal performance and biocompatibility of near-infrared light-responsive PDA@RES NPs. (a) Infrared thermal images and (b) photothermal response curves of PBS, PDA NPs, and PDA@RES NPs at different time points under near-infrared light (808 nm, 1.5 W/cm²) irradiation. (c) Temperature change curve of PDA@RES NPs (100 μg/mL) during natural cooling after 5 min of near-infrared light irradiation. (d) Temperature changes of different concentrations of PDA@RES NPs after 5 min of irradiation at 1.5 W/cm² intensity. (e) Temperature changes of PDA@RES NPs at a concentration of 100 μg/mL after 5 min of near-infrared light irradiation at different intensities. (f) Curves of 100 μg/mL PDA@RES NPs under 1.5 W/cm² near-infrared light irradiation for 5 heating/cooling cycles. (g) and (h) CCK-8 detection of L929 cells co-cultured with different concentrations of PDA@RES NPs (+/− NIR irradiation) for 1, 2, and 3 days (n = 3). Compared with 100 μg/mL PDA@RES: ns indicates no significant difference, $P \geq 0.05$. *$P < 0.05$, **$P < 0.01$, ***$P < 0.001$, ****$P < 0.0001$. (i) Live/dead cell staining images of L929 cells co-cultured with each group for 24 h (n = 3). Green, live cells; red, dead cells (n = 3).

efficiency (η) of PDA@RES was calculated to be 45.9% based on the heating-cooling profile and the energy balance equation (details provided in Fig. S4 in the ESM). This high efficiency confirms the suitability of PDA@RES as a potent PTT agent. In summary, the above results confirm that PDA@RES NPs possess outstanding photothermal conversion performance and high photothermal stability owing to their PDA core. The local, controllable mild hyperthermia generated under NIR irradiation serves as one of the

core driving forces for the platform to exert synergistic therapeutic effects and achieves the ideal result of optimizing the therapeutic microenvironment without damaging normal tissues.

2.2 *In vitro* biosafety of PDA@RES

Before conducting cell function experiments, evaluating the *in vitro* biocompatibility of nanomaterials is a critical prerequisite for their therapeutic application. Therefore, we rigorously evaluated the cytocompatibility of PDA@RES NPs. We first assessed the cell viability of L929 fibroblasts using the cell counting kit-8 (CCK-8) method. As shown in Figs. 2(g) and 2(h), within the concentration range of 0 to 100 μg/mL, whether or not NIR light irradiation was applied, after culturing for 1, 2, and 3 days, the viability of cells in each group showed no significant inhibition. This indicates that PDA@RES NPs do not significantly interfere with cell viability within the effective concentration range. Subsequently, we conducted more intuitive observations of the survival status of L929 cells cultured for 24 h in different groups through live/dead cell staining (Calcein-AM/propidium iodide (PI)). As shown in Fig. 2(i) and Fig. S5 in the ESM, after co-culturing with the control group, PDA alone group, PDA@RES group, and NIR+PDA@RES group, dense green fluorescence (live cells) was observed in all fields of view. The cells exhibited plump morphology with typical fibroblast spindle shapes, and almost no red fluorescence (dead cells) was observed. Moreover, the hemolysis assay confirmed the good hemocompatibility of PDA@RES NPs (Fig. S6 in the ESM). In summary, data from both the CCK-8, live/dead staining, and hemolysis assay indicate that PDA@RES NPs demonstrate good *in vitro* biocompatibility even in synergy with NIR photothermal effects. Based on the above results, we selected 100 μg/mL as the safe concentration for subsequent experiments.

2.3 *In vitro* antioxidant and anti-inflammatory capabilities of PDA@RES

To systematically evaluate the comprehensive biological effects of the PDA@RES nanoplatform in simulated pathological microenvironments *in vitro*, this study first focused on its core antioxidant capabilities (Figs. 3(a)–3(g)). At the chemical level, the 2,2'-azinobis-(3-ethylbenzthiazoline-6-sulphonate) (ABTS) free radical scavenging assay (Fig. 3(a)) confirmed that the NIR+PDA@RES group exhibited the highest scavenging efficiency, comparable to the positive control vitamin C (VC). This capability was fully validated in a RAW264.7 macrophage oxidative stress model induced by H_2O_2 and lipopolysaccharide (LPS). Treatment induced excessive intracellular ROS accumulation, as shown by strong green fluorescence from the DCFH-DA probe (Figs. 3(e) and 3(g)). This ROS overload rapidly depleted the endogenous antioxidant defense system within cells, manifested as a marked decline in the content of the key non-enzymatic antioxidant glutathione (GSH) (Fig. 3(b)) and the activity of the antioxidant enzyme superoxide dismutase (SOD) (Fig. 3(c)) [44]. The collapse of this defense system subsequently triggered severe lipid peroxidation, leading to significant accumulation of the damage end-product malondialdehyde (MDA) (Fig. 3(d)) [45]. However, intervention with the NIR+PDA@RES group demonstrated outstanding protective effects. It not only significantly reduced ROS fluorescence signals but also comprehensively restored GSH, SOD, and MDA levels to near-normal control group levels, thereby restoring cellular redox homeostasis.

A key downstream event of oxidative stress is mitochondrial damage and the exacerbation of inflammatory responses [46–48]. We evaluated changes in mitochondrial membrane potential (MMP) using the JC-1 probe (Figs. 3(f) and 3(h)). LPS treatment caused severe MMP damage, manifested as JC-1 dissociation from aggregates (red fluorescence) to monomers (green fluorescence), resulting in a decrease in the red/green fluorescence ratio (Fig. 3(h)). The NIR+PDA@RES group successfully restored high-level MMP in mitochondria by scavenging upstream ROS. This restoration of cellular homeostasis was ultimately reflected in the functional phenotype of macrophages [49, 50]. Quantitative real-time polymerase chain reaction (qRT-PCR) heatmap (Fig. 3(i)) analysis showed that LPS induced a strong M1-type pro-inflammatory response, manifested as high gene transcription levels of pro-inflammatory factors IL-6, TNF-α, and IL-1β, while suppressing transcription of pro-healing M2-type markers IL-10, TGF-β, and Arg-1. Intervention with NIR+PDA@RES significantly reversed this gene expression profile, strongly suppressing transcription of pro-inflammatory genes while upregulating levels of anti-inflammatory and pro-healing genes.

Consistent with the gene expression results, the protein expression levels of M1-type pro-inflammatory markers (TNF-α, IL-6, and IL-1β) were significantly reduced following NIR+PDA@RES intervention (Figs. 4(a)–4(d)). In the detection of anti-inflammatory proteins, the expression of M2-type markers IL-10, TGF-β, and Arg-1 in the LPS group was at extremely low levels. In contrast, NIR+PDA@RES intervention most powerfully promoted the synthesis and expression of these functional proteins, displaying the strongest green fluorescence signals (Figs. 4(e)–4(h)). These findings from mRNA to protein levels collectively confirm that the PDA@RES nanoplatform under NIR light response can efficiently suppress the pro-inflammatory response of macrophages and remodel them into a pro-healing M2 phenotype [51].

2.4 Transcriptomic analysis of PDA@RES anti-inflammatory mechanisms

To further elucidate the deep molecular mechanisms by which this nanoplatform reverses inflammation-induced pathological microenvironments, we performed transcriptomic sequencing (RNA sequencing) on macrophages in the LPS group and those stimulated with LPS followed by treatment with NIR+PDA@RES NPs. Principal component analysis (PCA) results depicted distinctly different gene expression profiles between the LPS group and the NIR+PDA@RES group (Fig. 5(a)), indicating clear transcriptomic separation between the two groups. To deeply investigate its molecular mechanisms, we subsequently identified differentially expressed genes (DEGs). Volcano plots (Fig. 5(b)) and clustering heatmaps (Fig. 5(c)) visually demonstrated this significant difference. Compared with the LPS group, NIR+PDA@RES treatment resulted in extensive reprogramming of gene expression levels. Encouraged by the evident transcriptomic changes, we subsequently performed Gene Ontology (GO) and Kyoto Encyclopedia of Genes and Genomes (KEGG) enrichment analyses to explore the functional characteristics of these DEGs. GO enrichment analysis (Fig. 5(d)) results showed that these differentially expressed genes were significantly enriched in mitochondrion-related terms in cellular components (CC) and in ATP binding in molecular functions (MF), preliminarily indicating that mitochondrial function and energy metabolism are core targets of this platform's intervention. Based on this, KEGG pathway enrichment analysis (Fig. 5(e)) further identified specific regulatory pathways. We found that entries related to AMPK signaling

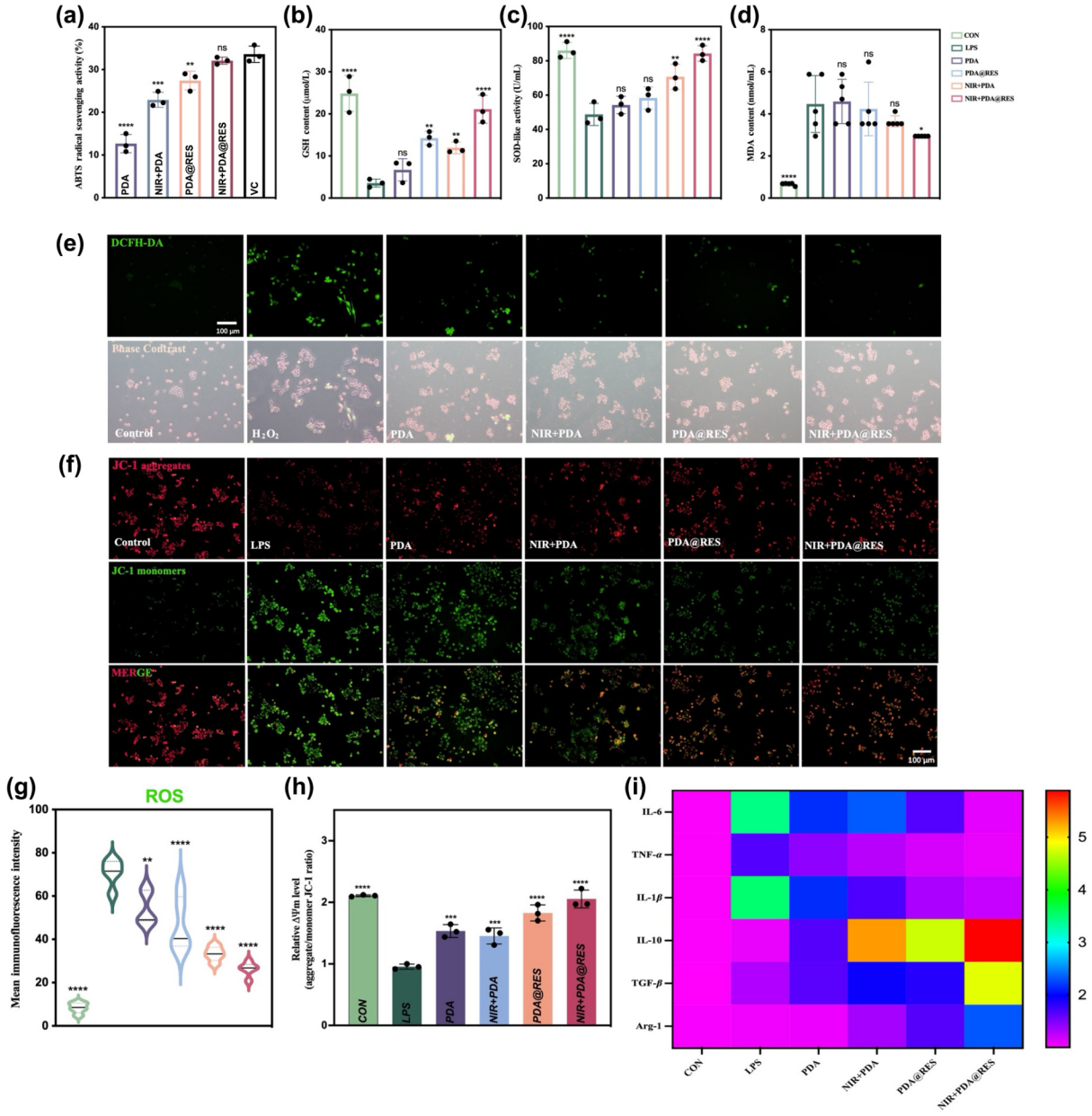

Figure 3 Determination of *in vitro* antioxidant and anti-inflammatory capabilities of near-infrared light-responsive PDA@RES NPs. (a) ABTS free radical scavenging assay. Compared with VC control group: ns indicates no significant difference, $P \geq 0.05$. $^{*}P < 0.05$, $^{**}P < 0.01$, $^{***}P < 0.001$, $^{****}P < 0.0001$ ($n = 3$). (b) Detection of intracellular reduced glutathione content in RAW264.7 cells ($n = 3$). (c) Detection of intracellular superoxide dismutase-like activity ($n = 3$). (d) Detection of trace intracellular malondialdehyde content ($n = 5$). (e) Intracellular ROS fluorescence images and (g) semi-quantitative analysis ($n = 5$). (f) Mitochondrial membrane potential fluorescence images and (h) semi-quantitative analysis ($n = 3$). (i) qRT-PCR detection of mRNA expression levels of pro-inflammatory cytokines (interleukin-6 (IL-6), tumor necrosis factor-alpha (TNF-α), and IL-1β) and anti-inflammatory cytokine markers (IL-10, transforming growth factor-beta (TGF-β), and Arg-1) ($n = 3$). In panels (b)–(d), (g), and (h): ns indicates no significant difference, $P \geq 0.05$. $^{*}P < 0.05$, $^{**}P < 0.01$, $^{***}P < 0.001$, $^{****}P < 0.0001$, compared with LPS group.

pathway and cellular senescence were both significantly enriched. We also conducted Gene Set Enrichment Analysis (GSEA). As shown in Figs. 5(f) and 5(g), compared with the LPS group, the AMPK signaling pathway was significantly activated in the NIR+PDA@RES treatment group, while the cellular senescence pathway was significantly suppressed. To visually confirm the expression changes of key genes involved in these pathways, the circular heatmap (Fig. S7 in the ESM) further highlighted that inflammation- and senescence-related genes were significantly downregulated, while mitochondrial function-associated genes were upregulated in the NIR+PDA@RES group compared to the LPS group.

The series of bioinformatics analysis results collectively pointed to a clear mechanistic hypothesis: the intervention effect of NIR+PDA@RES is driven by AMPK signaling pathway activation, which subsequently regulates key mitochondrial homeostasis and ultimately achieves reversal of cellular senescence. Guided by this transcriptomic analysis, we subsequently conducted in-depth experimental validation of this core mechanistic axis of AMPK-mitochondrial homeostasis-cellular senescence.

Before examining the molecular signaling, we first investigated the intracellular trafficking behavior of the nanoplatform, as the

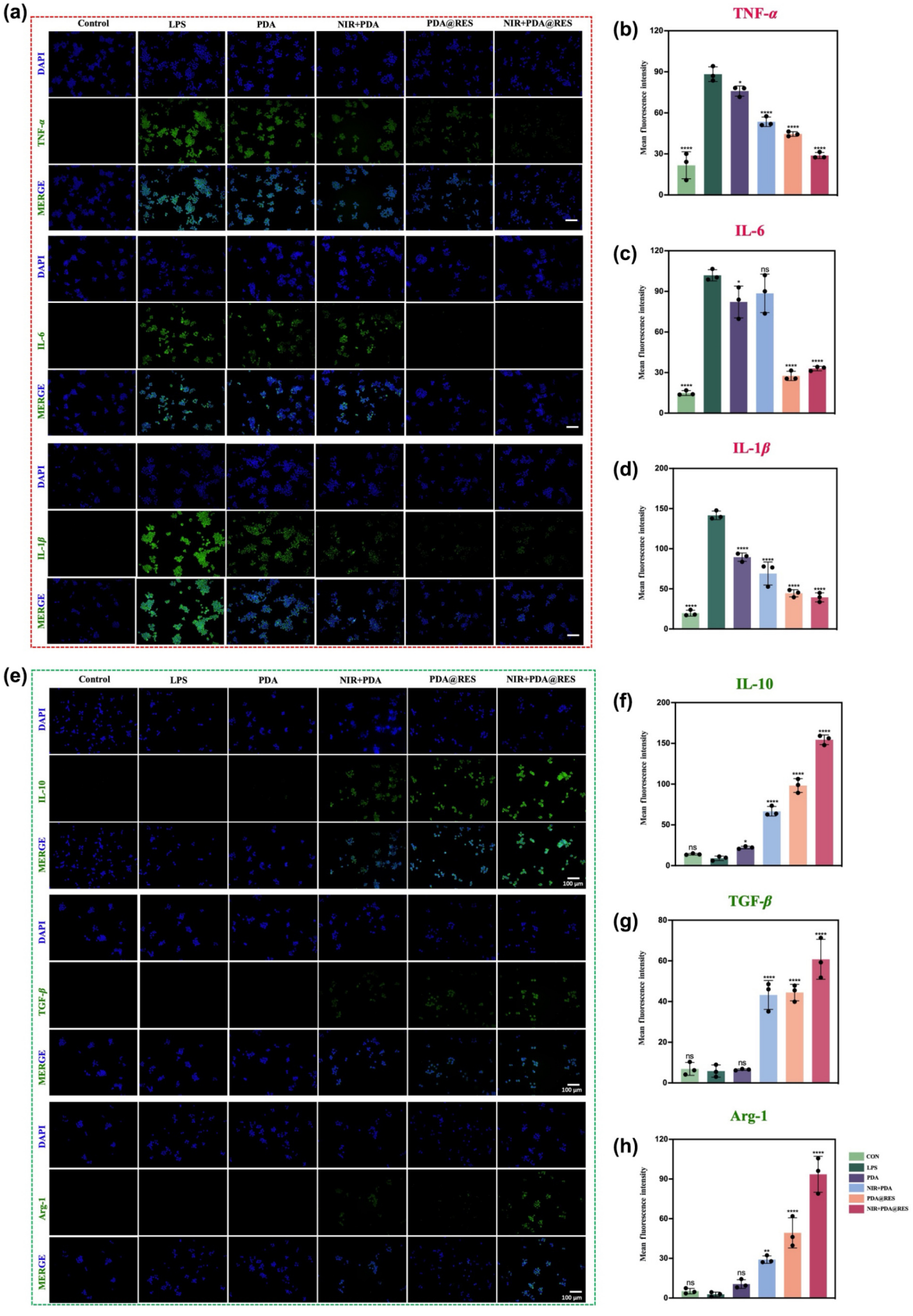

Figure 4 *In vitro* anti-inflammatory capability of near-infrared light-responsive PDA@RES NPs. (a) Immunofluorescence staining of pro-inflammatory cytokine marker proteins and semi-quantitative analysis of (b) TNF-α, (c) IL-6, and (d) IL-1β (n = 3). (e) Immunofluorescence staining of anti-inflammatory cytokine marker proteins and semi-quantitative analysis of (f) IL-10, (g) TGF-β, and (h) Arg-1 (n = 3). ns indicates no significant difference, $P \geq 0.05$. *$P < 0.05$, **$P < 0.01$, ***$P < 0.001$, ****$P < 0.0001$, compared with LPS group.

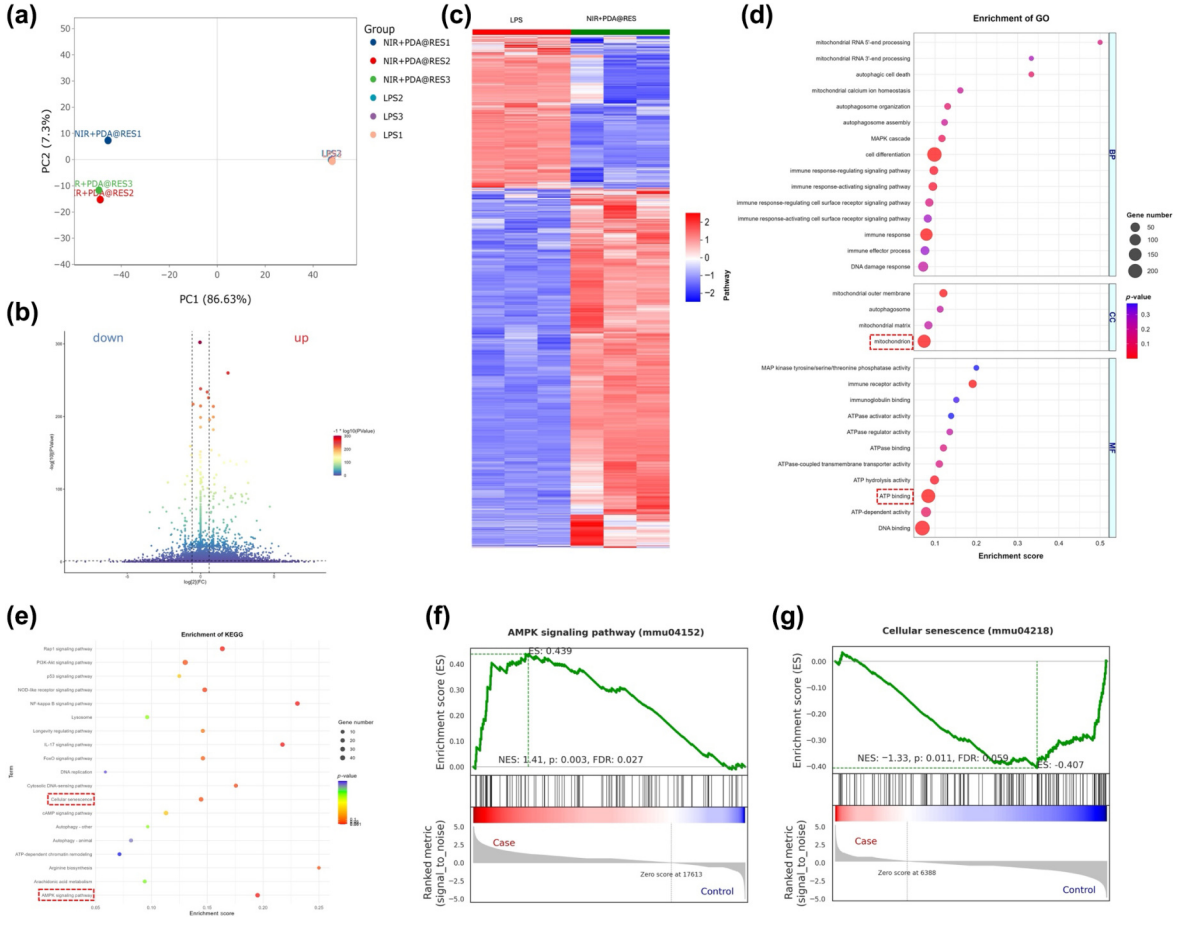

Figure 5 Mechanistic exploration through bioinformatics analysis based on RNA sequencing and experimental validation. (a) Principal component analysis. (b) Identification of DEGs. (c) Gene expression heatmap between LPS group and NIR+PDA@RES NPs group. (d) GO and (e) KEGG enrichment analysis results. (f) GSEA results for AMPK and (g) cellular senescence signaling pathways.

cytosolic availability of RES is the physical prerequisite for activating the cytoplasmic AMPK pathway. Bio-TEM analysis (Fig. S8 in the ESM) was employed to visualize the dynamic "uptake-and-escape" process. As shown in Fig. S8(a) in the ESM, PDA@RES nanoparticles were internalized via endocytosis within 1 h of incubation. Subsequently, a significant accumulation of nanoparticles within membrane-bound lysosomes was observed at 5 h (Fig. S8(b) in the ESM). Most distinctively, upon NIR irradiation, the photothermal effect facilitated the successful release of nanoparticles from lysosomes into the cytoplasm (Fig. S8(c) in the ESM). This cytosolic distribution is critical, as it ensures that RES is effectively delivered to the intracellular environment to activate the cytoplasmic AMPK signaling pathway. With the intracellular delivery confirmed, we examined the activation status of core members of the AMPK pathway (Fig. 6). Under LPS-induced energy stress, cells attempted to initiate phosphorylation of AMPKα (p-AMPKα) as a compensatory response [52, 53], but Western blot results (Figs. 6(a), 6(b), and 6(e)) showed that this activation was insufficient. However, intervention with NIR+PDA@RES could potently activate p-AMPKα. AMPK activation is closely associated with its key downstream effectors SIRT 1 and PGC-1α [54]. We found that the LPS-induced downregulation of SIRT1 protein (Figs. 6(a) and 6(c)) and mRNA (Fig. 6(i)) levels was significantly reversed by NIR+PDA@RES. Activation of the AMPK/SIRT1 axis further converges on PGC-1α, the master regulator of mitochondrial biogenesis and function [55]. As shown in Figs. 6(a) and 6(d), PGC-1α protein expression was severely suppressed in the LPS model, whereas NIR+PDA@RES treatment restored its expression levels. This critical upregulation was also cross-validated at both protein and transcriptional levels through immunofluorescence staining (Figs. 6(f) and 6(f)) and qRT-PCR (Fig. 6(h)). As the master switch for mitochondrial biogenesis, PGC-1α activation initiated the downstream reconstruction program [56]. qRT-PCR results showed that upregulation of PGC-1α (Fig. 6(h)) successfully activated transcription of its downstream nuclear respiratory factor (NRF1) (Fig. 6(o)) and mitochondrial transcription factor A (TFAM) (Fig. 6(p)) [57]. This initiation of the transcriptional program was ultimately effectively translated into key proteins involved in mitochondrial respiration and energy generation, such as ATP5A (Complex V) and COXIV (Complex IV), whose protein expression (Figs. 6(j)–6(l), and Fig. S9 in the ESM) was significantly restored.

This structural reconstruction directly led to functional recovery. As shown in Figs. 7(a) and 7(b), LPS treatment caused cells to fall into an energy crisis characterized by sharp declines in ATP production and nicotinamide adenine dinucleotide reduced form/oxidized form (NADH/NAD$^+$) ratio, whereas NIR+PDA@RES intervention successfully restored these two key energy indicators to normal levels through mitochondrial function reconstruction. However, biogenesis alone is insufficient to restore homeostasis; the large number of damaged mitochondria induced by LPS must also be cleared. LPS treatment caused catastrophic

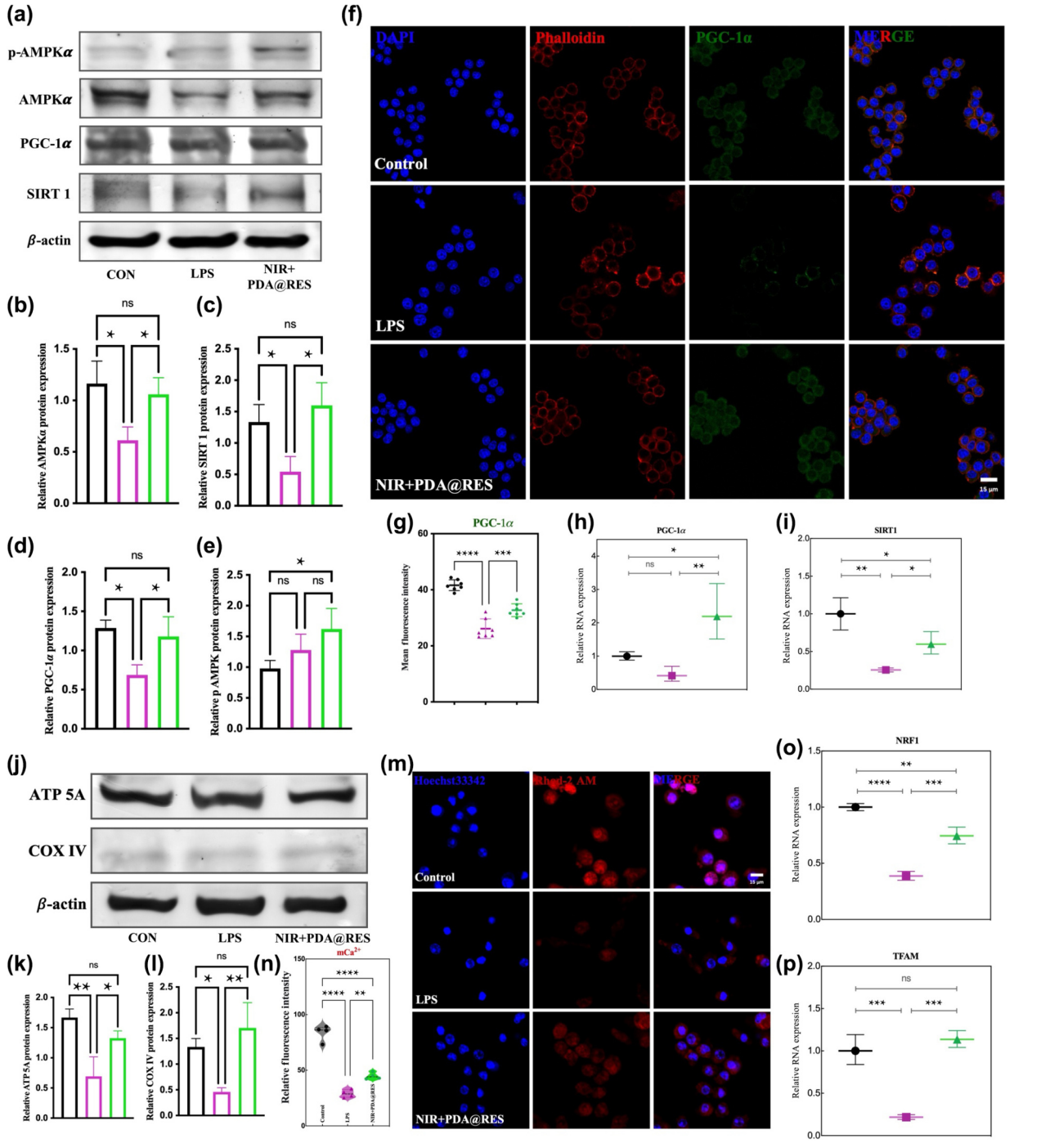

Figure 6 Near-infrared light-responsive PDA@RES NPs restore mitochondrial homeostasis by activating the AMPK signaling pathway. (a) Western blot results and statistical analysis of AMPK signaling pathway-related proteins: (b) AMPKα, (c) sirtuin 1 (SIRT1), (d) PGC-1α, and (e) AMPK proteins (n = 3). (f) PGC-1α immunofluorescence staining and (g) statistical analysis (n = 3). qRT-PCR detection of mRNA expression levels of genes related to the AMPK signaling pathway: (h) PGC-1α and (i) SIRT1 (n = 3). (j) Western blot results and statistical analysis of mitochondrial biogenesis-related proteins: (k) ATP5A and (l) COX IV (n = 3). (m) Mitochondrial calcium ion staining and (n) statistical analysis (n = 4). qRT-PCR detection of mRNA expression levels of mitochondrial biogenesis-related genes: (o) NRF1 and (p) TFAM (n = 3). ns indicates no significant difference, $P \geq 0.05$. *$P < 0.05$, **$P < 0.01$, ***$P < 0.001$, ****$P < 0.0001$.

mitochondrial damage (Fig. 7) [58]. TEM images (Fig. 7(e)) clearly showed that mitochondria in the LPS group exhibited matrix swelling and abnormal or even depleted cristae morphology. Functionally, this manifested as excessive accumulation of mitochondrial ROS (mtROS) (Figs. 7(c) and 7(d)) and significant reduction in mitochondrial calcium ion ($mtCa^{2+}$) levels (Figs. 6(m) and 6(n)). In response to this damage, NIR+PDA@RES intervention initiated the mitophagy program in parallel. qRT-PCR showed that mRNA levels of key mitophagy genes PINK1 (Fig. 7(g)) and PRKN (Fig. 7(f)) were significantly upregulated. This molecular activation was confirmed at the ultrastructural level. Biological transmission electron microscopy (Fig. 7(e)) captured clear autophagosome structures (blue arrows) in the NIR+ PDA@RES group. This synergistic strategy of autophagy and

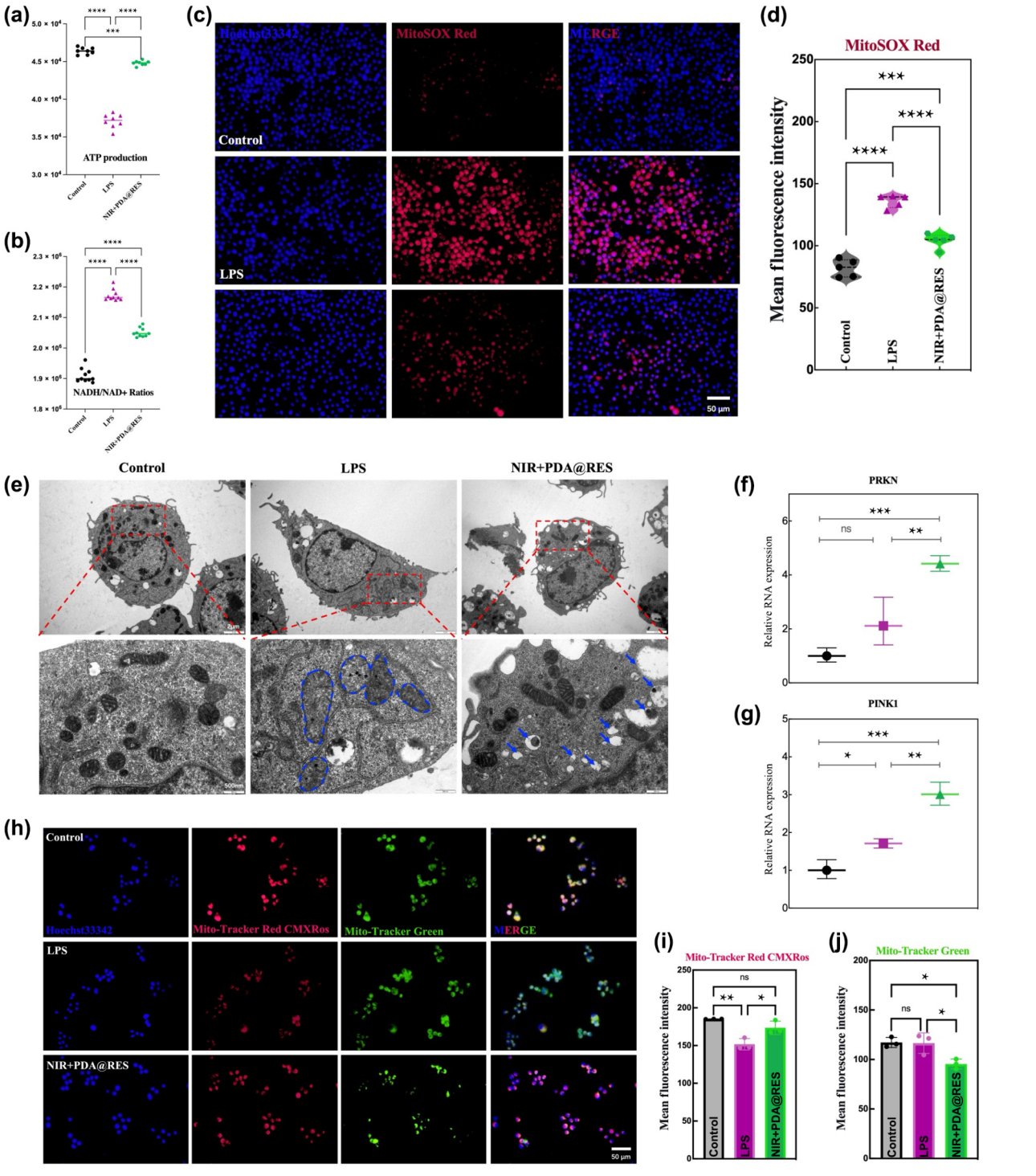

Figure 7 Near-infrared light-responsive PDA@RES NPs restore mitochondrial homeostasis. (a) ATP production (n = 8). (b) NADH/NAD$^+$ ratio (n = 10). (c) Mitochondrial ROS staining and (d) statistical analysis (n = 5). (e) Transmission electron microscopy analysis of mitochondrial morphology. The control group shows normal mitochondrial morphology. The LPS group shows mitochondrial matrix swelling, abnormal cristae morphology, and a small amount of mitochondrial autophagy. The treatment group shows recovery of mitochondrial matrix swelling, with most damaged mitochondria undergoing autophagy and autophagosome structures appearing. qRT-PCR detection of mRNA expression levels of mitophagy-related cytokines (f) PRKN and (g) PINK1 (n = 3). (h) Fluorescence imaging of mitochondrial staining and statistical analysis of (i) MitoTracker Red CMXRos and (j) MitoTracker Green, green labels all mitochondria in cells, red labels biologically active mitochondria in cells (n = 3). ns indicates no significant difference, $P \geq 0.05$. *$P < 0.05$, **$P < 0.01$, ***$P < 0.001$, ****$P < 0.0001$.

biogenesis was ultimately reflected in the restoration of the healthy mitochondrial pool. MitoTracker double staining (Figs. 7(h)–7(j)) results showed that the proportion of high-activity, high-membrane-potential (MitoTracker Red CMXRos) mitochondria in the LPS group sharply declined, whereas NIR+PDA@RES treatment successfully restored the population of active mitochondria (Red) and total mitochondrial mass (Green), indicating that cellular oxidative stress and ionic imbalance were corrected and

mitochondrial homeostasis was remodeled.

Severe imbalance in mitochondrial homeostasis and persistent oxidative stress are key driving factors for inducing cellular senescence [59, 60]. Therefore, we finally validated LPS-induced cellular senescence and its reversal (Fig. 8). Under LPS stimulation, FOXO3A expression was significantly upregulated. Immunofluorescence (Figs. 8(d) and 8(h)) showed enhanced protein fluorescence intensity, which was completely consistent with mRNA (Fig. 8(e)) detected by qRT-PCR and total protein (Figs. 8(a) and 8(b)) detected by Western blot showing significantly upregulated results. The activated FOXO3A pathway subsequently initiated cell cycle inhibition programs [61]. qRT-PCR (Figs. 8(f) and 8(g)) and Western blot (Figs. 8(a) and 8(d), and Fig. S9 in the ESM) results confirmed that expression of cell cycle inhibitory factors p21 and p16 was upregulated in the LPS group, indicating that cells had entered a senescent state [62]. However, NIR+PDA@RES intervention successfully reversed this process. Because the upstream AMPK pathway was activated (Fig. 6) and mitochondrial homeostasis was remodeled (Fig. 7), the FOXO3A activation signal was abrogated. Immunofluorescence (Figs. 8(d) and 8(h)) showed that FOXO3A fluorescence intensity was significantly suppressed, and its total protein and mRNA expression (Figs. 8(a), 8(b), and 8(e)) also recovered. Finally, expression of p21 and p16 (Figs. 8(a), 8(c), 8(f), and 8(g)) was also correspondingly suppressed, strongly demonstrating that the platform successfully reversed LPS-induced cellular senescence by remodeling mitochondrial homeostasis. Additionally, SA-β-gal staining results provided qualitative phenotypic evidence supporting the reversal of senescence (Fig. S10 in the ESM).

2.5 Assessment of angiogenic capacity driven by immune microenvironment remodeling

The fundamental pathological mechanism underlying the difficulty in healing chronic wounds lies in the persistent inflammatory microenvironment suppressing endothelial cell activity, leading to stagnation of angiogenesis [63, 64]. In the aforementioned experiments, we demonstrated that the PDA@RES nanoplatform under near-infrared light irradiation can effectively scavenge ROS and drive macrophage polarization toward a pro-healing M2 phenotype (Figs. 3 and 4). Given that M2-type macrophages are the primary cellular source of angiogenic factors such as vascular endothelial growth factor (VEGF) and TGF-β, their phenotypic reversal is a prerequisite for initiating subsequent tissue repair [65]. Therefore, we further investigated the recovery of vascular endothelial cell function based on PDA@RES remodeling of cellular homeostasis and the microenvironment.

Angiogenesis is a cascade process dependent on endothelial cell migration, proliferation, and luminal spatial assembly [66]. We evaluated the effect of PDA@RES on the migratory behavior of human umbilical vein endothelial cells (HUVECs) through scratch assays (Figs. 9(a) and 9(b)) and Transwell assays (Figs. 9(c) and 9(d)). Experimental results showed that cells in the control group had limited migration capacity due to lack of effective microenvironmental support, while the NIR+PDA@RES treatment group exhibited significantly enhanced migratory activity and

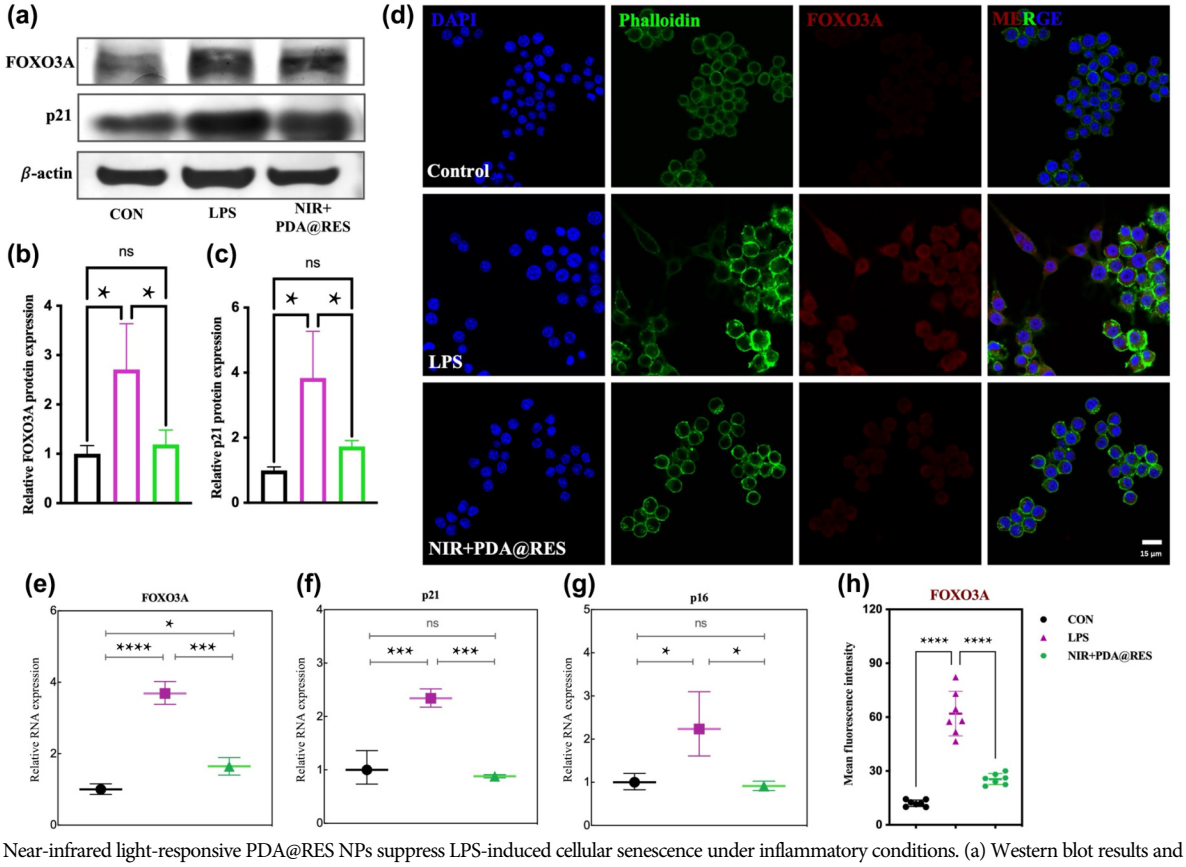

Figure 8 Near-infrared light-responsive PDA@RES NPs suppress LPS-induced cellular senescence under inflammatory conditions. (a) Western blot results and statistical analysis of cellular senescence signaling pathway-related proteins: (b) forkhead box O3A (FOXO3A) and (c) p21 (n = 3). (d) FOXO3A immunofluorescence staining and (h) statistical analysis (n = 3). qRT-PCR detection of mRNA expression levels of cytokines related to the cellular senescence signaling pathway: (e) FOXO3A, (f) p21, and (g) p16 (n = 3). ns indicates no significant difference, $P \geq 0.05$. *$P < 0.05$, **$P < 0.01$, ***$P < 0.001$, ****$P < 0.0001$.

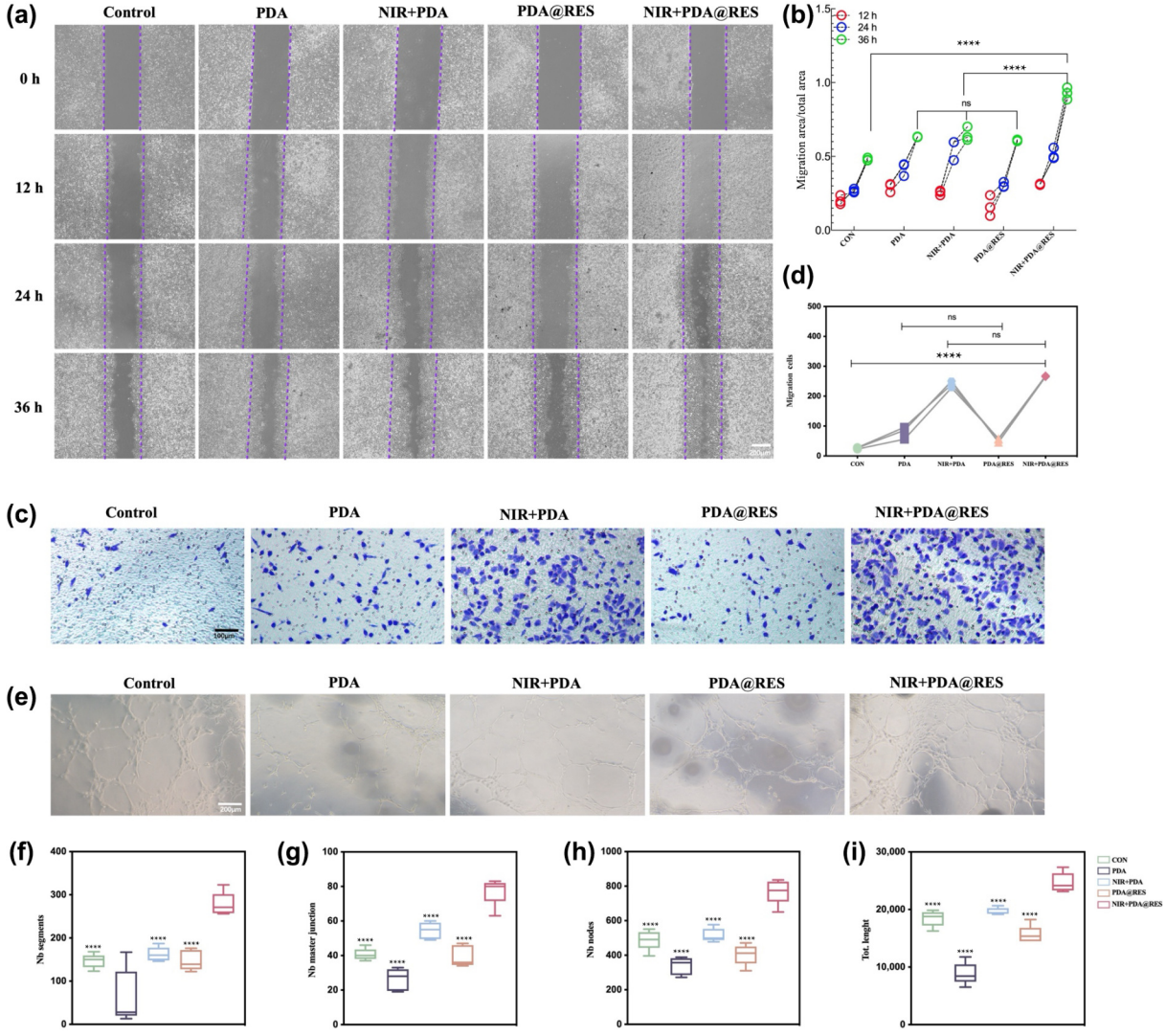

Figure 9 Near-infrared light-responsive PDA@RES NPs promote HUVECs migration and tube formation. (a) Measurement of horizontal migration ability of HUVECs at 12, 24, and 36 h through scratch assay. (b) Statistical analysis of migration rate at 36 h (n = 3). (c) Transwell vertical migration assay of HUVECs and (d) statistical analysis (n = 3). (e) HUVECs tube formation assay results, and statistical analysis of (f) the number of tube segments, (g) number of nodes, (h) number of master junctions, and (i) total tube length (n = 5). ns indicates no significant difference, $P \geq 0.05$. *$P < 0.05$, **$P < 0.01$, ***$P < 0.001$, ****$P < 0.0001$, compared with NIR+PDA@RES group.

sustained proliferative potential (Fig. S11 in the ESM), with both wound healing rate and the number of cells crossing the Transwell microporous membrane being significantly higher than all other groups. This restoration of cellular motility laid the foundation for subsequent vascular construction. Further Matrigel tube formation assays (Figs. 9(e)–9(i)) confirmed that the NIR+PDA@RES group induced HUVECs to rapidly assemble into structurally complete, complexly branched capillary-like networks. Topological quantitative analysis showed that this group presented optimal results in key morphological indicators such as number of tube segments (Nb segments), number of nodes (Nb nodes), and total tube length (Tot length). This phenomenon indicates that the nanoplatform, by restoring intracellular mitochondrial homeostasis and simulating a permissive regenerative microenvironment, effectively lifted the suppression of endothelial cell tube formation capacity by the pathological state.

To decipher the molecular basis of this immune-vascular cascade effect, we examined core signaling pathways related to angiogenesis (Fig. 10). Improvement of the immune microenvironment is usually accompanied by cascade amplification of pro-angiogenic signals. qRT-PCR and immunofluorescence analysis showed that the NIR+PDA@RES group significantly upregulated the expression of hypoxia-inducible factor-1α (HIF-1α) (Fig. 10(e)). As an upstream core transcription factor that senses cellular metabolic status and regulates angiogenesis, HIF-1α activation directly drives the transcription and translation of its downstream target gene *VEGF* (Figs. 10(a), 10(b), and 10(f)). High expression of VEGF provides endothelial cells with necessary proliferation and migration signals, explaining the excellent migratory phenotype observed in the aforementioned experiments. Meanwhile, the expression level of CD31, a key marker reflecting vascular structural stability and intercellular connections, was also synchronously and significantly elevated [67, 68]. Taken together, these results demonstrate that the PDA@RES nanoplatform does not promote angiogenesis in isolation but rather activates the HIF-1α/VEGF signaling axis by lifting oxidative stress and inflammation's blockade

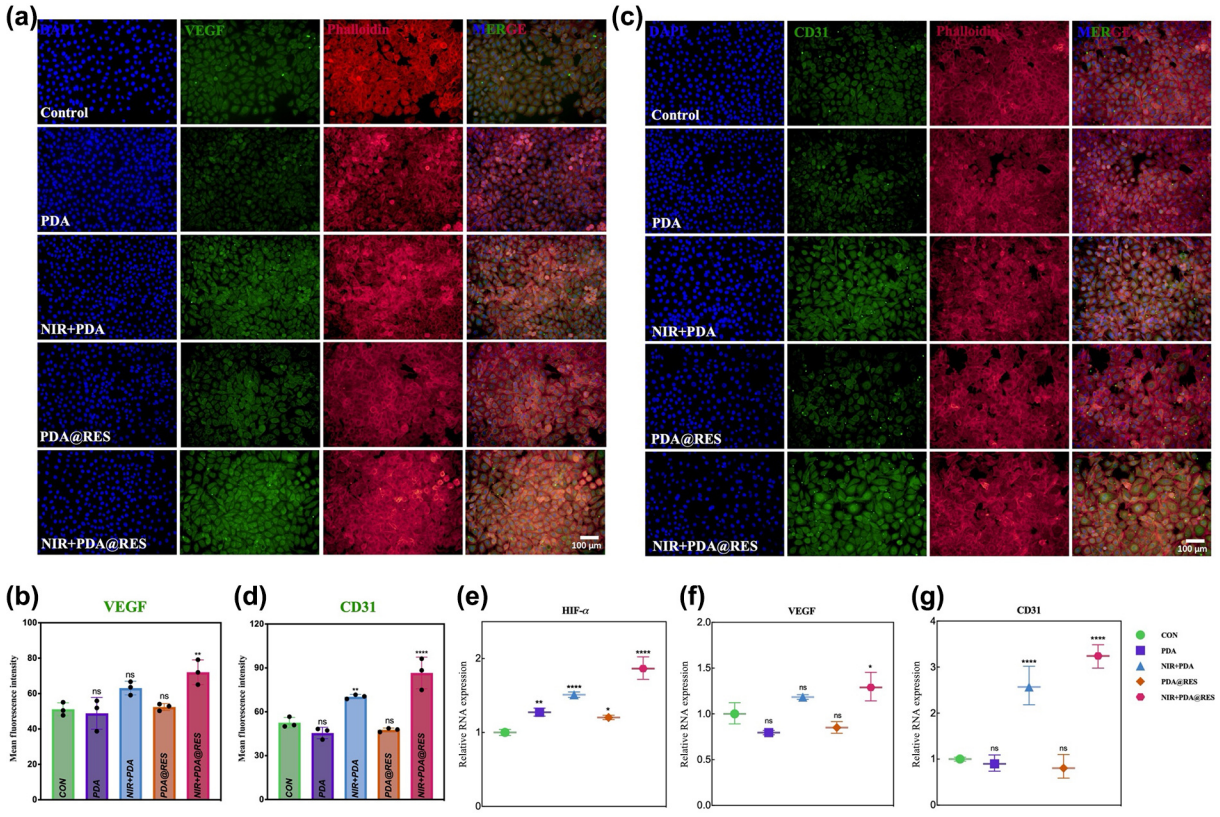

Figure 10 Detection of angiogenesis-related proteins and genes by near-infrared light-responsive PDA@RES NPs. Immunofluorescence staining and statistical analysis of angiogenesis-related proteins (a) and (b) VEGF, and (c) and (d) CD31 (n = 3). qRT-PCR detection of mRNA expression levels of angiogenesis-related genes: (e) HIF-1α, (f) VEGF, and (g) CD31 (n = 3). ns indicates no significant difference, $P \geq 0.05$. *$P < 0.05$, **$P < 0.01$, ***$P < 0.001$, ****$P < 0.0001$, compared with CON group.

of cellular function, thereby achieving efficient transmission from immune microenvironment remodeling to functional vascular regeneration.

2.6 Therapeutic effect of PDA@RES combined with hyaluronic acid (HAMA) hydrogel system on diabetic rat wounds

To verify the therapeutic potential of PDA@RES NPs in complex physiological environments based on *in vitro* studies, we constructed an injectable, near-infrared light-responsive nanocomposite hydrogel. We selected methacrylated HAMA, which possesses excellent biocompatibility and photocurability, as the matrix [69]. The chemical synthesis of HAMA and its internal porous structure loaded with nanoparticles were confirmed by FTIR (Fig. S12 in the ESM) and scanning electron microscopy (SEM) (Fig. S13 in the ESM), respectively. Beyond its role as a delivery vehicle, HAMA provides essential biological and structural advantages as a biomimetic scaffold. Hyaluronic acid is a primary physiologically relevant component of the native extracellular matrix, offering a microenvironment that inherently supports cellular processes such as adhesion and proliferation [70]. While native hyaluronic acid is prone to rapid degradation, the crosslinked network of HAMA significantly enhances its structural integrity and durability under physiological conditions [71]. Furthermore, the porous architecture of the HAMA hydrogel facilitates nutrient transport and provides the necessary physical support for organized tissue remodeling. The HAPR hydrogel system was prepared by loading the PDA@RES nanoplatform into the HAMA matrix (Fig. 11(b)).

Following the protocol shown in Fig. 11(a), we constructed diabetic rat models by injecting streptozotocin (STZ) and created 1.5-cm-diameter full-thickness skin defects on their backs. Animals were divided into four groups: Control, HAMA (blank hydrogel), HAPR (HAMA+PDA@RES), and HAPRN (HAMA+PDA@RES+ near-infrared irradiation). During treatment, the HAPRN group exhibited a rapid and stable *in vivo* photothermal response as monitored by thermal imaging (Fig. S14 in the ESM). Macroscopic healing results (Figs. 11(c)–11(e)) showed that the HAPRN group exhibited the most significant healing effect. At day 10, wounds in the HAPRN group had largely closed and achieved complete healing by day 14, with healing rates significantly higher than all other control groups, whereas wounds in the Control and HAMA groups remained unhealed, confirming the excellent efficacy of the NIR-responsive synergistic therapeutic strategy *in vivo*. Simultaneously, histological examination of major organs (heart, liver, spleen, lung, kidney) revealed no significant pathological abnormalities, confirming the systemic biosafety of the treatment (Fig. S15 in the ESM).

We subsequently evaluated the quality of healed tissue through histological analysis (Figs. 12(a) and 12(b)). At day 14, hematoxylin and eosin (H&E) staining showed that the Control and HAMA groups still had obvious wound gaps and extensive inflammatory cell infiltration. In contrast, wounds in the HAPRN group were completely covered by structurally intact newly formed epidermis with a clear dermal layer structure. Most critically, we observed clear regenerative structures of hair follicles and other skin

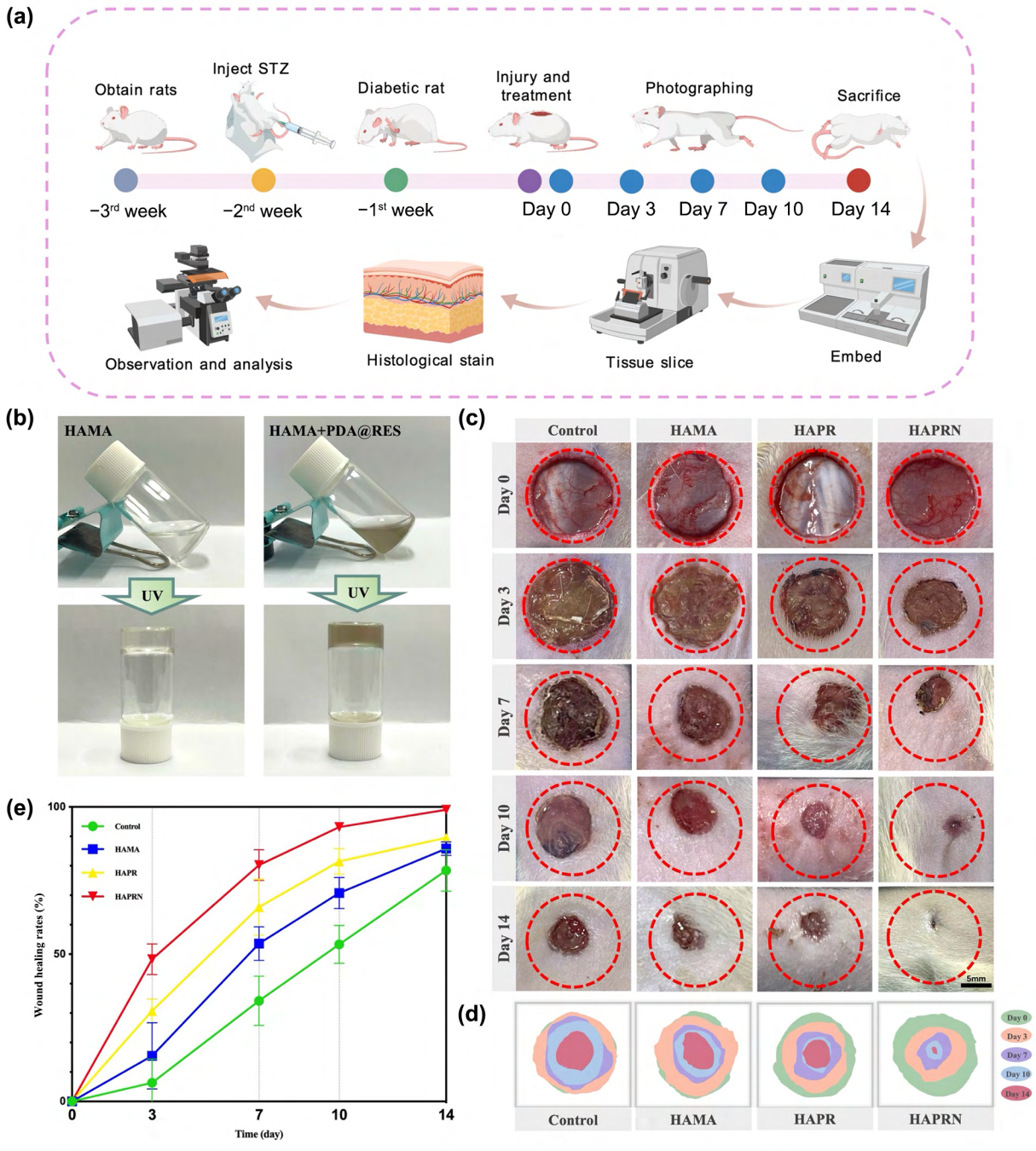

Figure 11 *In vivo* experiments of near-infrared light-responsive PDA@RES NPs promoting chronic wound healing. (a) Animal *in vivo* experimental protocol. (b) Construction of HAMA hydrogel system loaded with PDA@RES. (c) Photographs of wounds in different groups on days 0, 3, 7, 10, and 14, (d) schematic diagram of area fitting, and (e) statistical analysis of wound healing rate ($n = 3$).

appendages in the newly formed tissue of the HAPRN group at day 14, which are typically absent in scar repair [72–74]. Masson's trichrome staining further confirmed high-quality tissue remodeling. Unlike the sparse and disorganized collagen deposition in the Control group, the HAPRN group showed the densest, mature, and well-organized collagen network at day 14, strongly indicating that it promoted true, high-quality regenerative healing.

To investigate the cellular mechanisms by which PDA@RES promotes regeneration, we performed immunofluorescence analysis on healed tissues. Healing stagnation in chronic wounds is usually attributed to persistent inflammation dominated by M1-type macrophages. We first examined phenotypic transformation of the immune microenvironment (Figs. 12(c), 12(e), and 12(f)). Results showed that wounds in the Control and HAMA groups were filled with large numbers of inducible nitric oxide synthase (iNOS)-positive M1-type pro-inflammatory macrophages, indicating that the inflammatory state had not subsided. In contrast, the HAPRN group, through the synergistic action of photothermal and resveratrol, successfully broke this pathological impasse, with iNOS expression suppressed to the lowest level, while CD206 (M2 marker) representing the pro-healing phenotype showed overwhelmingly high expression. This successful reversal from pro-

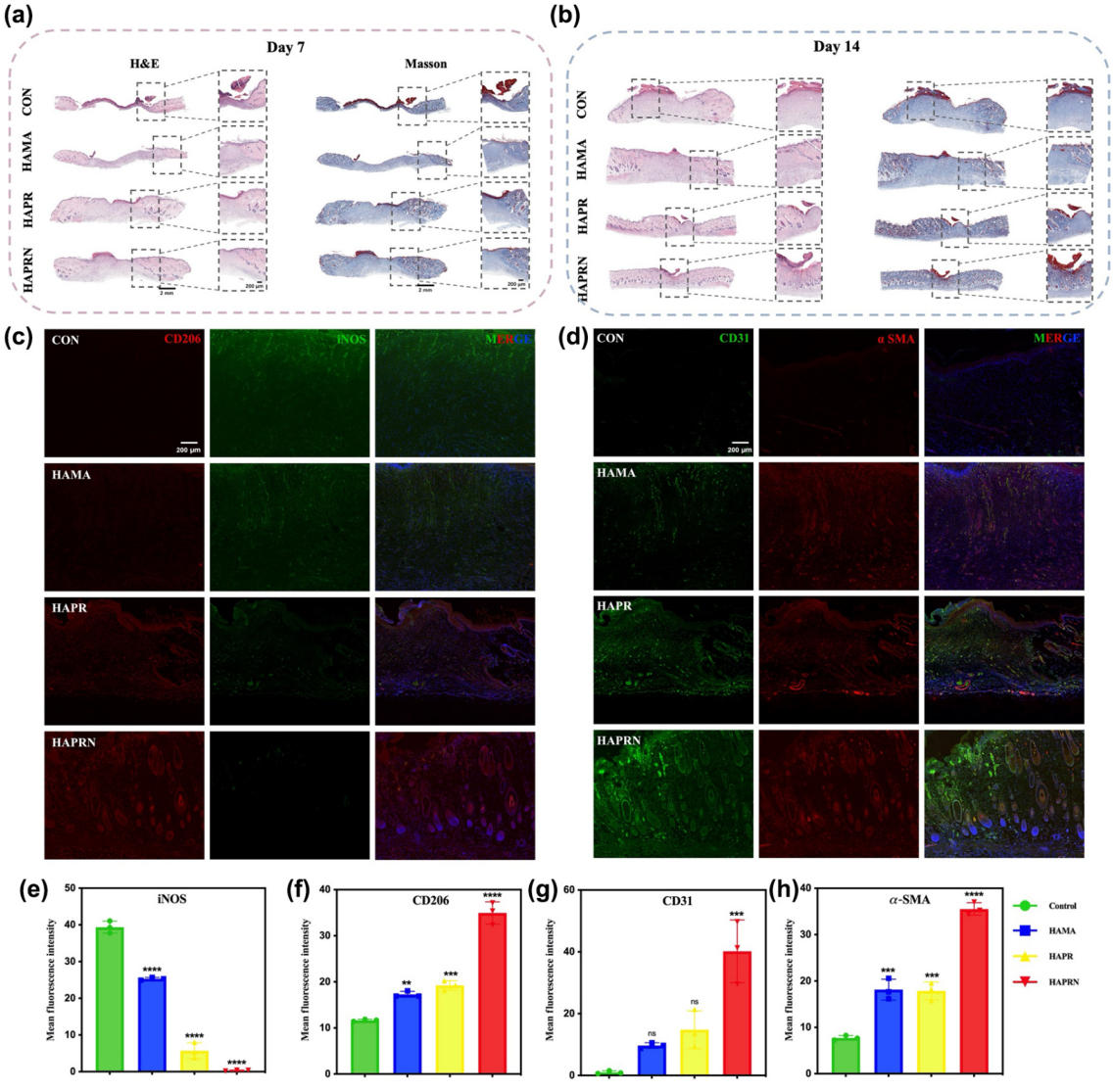

Figure 12 Histological and immunological analysis of near-infrared light-responsive PDA@RES NPs in *in vivo* experiments. H&E and Masson staining of wound tissues from different groups at days (a) 7 and (b) 14. (c) Immunofluorescence staining of macrophage markers, and statistical analysis of (e) M1 macrophage marker iNOS and (f) M2 macrophage marker CD206 ($n = 3$). (d) Immunofluorescence staining of angiogenesis-related proteins and statistical analysis of (g) CD31 and (h) α-SMA ($n = 3$). ns indicates no significant difference, $P \geq 0.05$. *$P < 0.05$, **$P < 0.01$, ***$P < 0.001$, ****$P < 0.0001$.

inflammatory to pro-healing phenotype is a necessary prerequisite for initiating downstream vascular reconstruction programs. Accompanying the improvement of the immune microenvironment, the HAPRN group demonstrated excellent vascular regeneration capacity. Through double staining of the vascular endothelial marker CD31 and alpha-smooth muscle actin (α-SMA, Figs. 12(d), 12(g), and 12(h)), we found that this group not only showed the highest vascular density but also exhibited high co-localization of CD31 and α-SMA. This indicates that this strategy, by remodeling the immune microenvironment, effectively lifted inflammation's suppression of angiogenesis and subsequently induced the formation of structurally mature and functionally complete vascular networks. It is worth noting that different therapeutic strategies offer distinct and complementary benefits. While recent scaffold-based systems such as the epigallocatechin gallate (EGCG)-releasing fibers reported by An et al. [75] excel in providing long-term structural support and sustained immunomodulation via passive release, our PDA@RES nanoplatform explores a spatiotemporal on-demand modality. This NIR-triggered approach allows for high-concentration drug delivery precisely during inflammatory peaks acting as a pulse therapy to break the pathological stalemate of chronic wounds which complements continuous dosing regimens. Furthermore, a unique thermal and biochemical synergy is achieved in our core-shell design where the mild hyperthermia generated by PDA not only triggers drug release but also potentially increases local blood perfusion and cellular membrane permeability. This mechanism maximizes the intracellular accumulation and mitochondrial remodeling efficacy of the released RES. Moving forward, investigating the long-term *in vivo* degradation kinetics of PDA residues in comparison to biodegradable polymers like poly(lactic-co-glycolic acid) (PLGA) will be essential to fully guarantee chronic safety for clinical translation.

3 Conclusions

This study aimed to address the vicious cycle among persistent

inflammation, mitochondrial dysfunction, and cellular senescence in chronic wounds. We successfully constructed an NIR light-responsive polydopamine-resveratrol (PDA@RES) core-shell nanoplatform. Mechanistically, upon activation by near-infrared light, this nanoplatform synergistically exerts photothermal effects and drug activity to precisely target and activate the AMPK/PGC-1α signaling axis. Activation of this pathway triggers a dual therapeutic cascade. First, it initiates programmed mitochondrial homeostasis remodeling. It mediates mitophagy through upregulation of PINK1 and PRKN genes, selectively clearing damaged mitochondria to alleviate oxidative stress. Simultaneously, it promotes mitochondrial biogenesis through upregulation of TFAM and NRF1 genes, replenishing healthy mitochondria and restoring cellular energy metabolism. Second, it suppresses FOXO3A, significantly downregulating expression of key markers such as p16 and p21, thereby efficiently reversing cellular senescence. *In vivo* experiments confirmed that homeostasis restoration at the cellular level effectively broke the pathological impasse of chronic wounds. This strategy first successfully remodeled the immune microenvironment from a pro-inflammatory (M1) state to a pro-healing (M2) state. The establishment of this permissive microenvironment subsequently drove the formation of high-quality mature vascular networks and ultimately significantly accelerated wound healing in diabetic rats. Most critically, we observed clear nascent hair follicle structures in the healed wounds, which represents the gold standard for distinguishing scar repair from true regenerative healing, strongly demonstrating that this strategy achieved high-quality functional skin reconstruction. Distinguished from traditional single-pathway interventions, this study pioneered a novel therapeutic strategy that couples programmed mitochondrial remodeling with reversal of cellular senescence mediated by a nanoplatform, laying a theoretical foundation for developing regenerative materials for other chronic inflammatory diseases characterized by metabolic dysfunction and senescence, such as osteoarthritis and neurodegenerative diseases.

4 Experimental

4.1 Materials and reagents

Dopamine hydrochloride (62-31-7) and sodium hyaluronate (H107141) were purchased from Shanghai Aladdin Biochemical Technology Co., Ltd. Resveratrol (1602105-100MG) was purchased from Merck Chemical Technology (Shanghai) Co., Ltd. Methacrylic anhydride (760-93-0) and sodium periodate (S817518) were purchased from Shanghai Macklin Biochemical Technology Co., Ltd. Tris-base (60102ES76) and Tris-HCl (60113ES76) were purchased from Shanghai Yeasen Biotechnology Co., Ltd. Anhydrous ethanol (64-17-5), formaldehyde (50-00-0), and ammonia water (1336-21-6) were purchased from Nanjing Chemical Reagent Co., Ltd.

Cell Counting Kit-8 (C0038), Calcein/PI Cell Viability and Cytotoxicity Detection Kit (C2015M), Reactive Oxygen Species Detection Kit (S0033S), Enhanced Mitochondrial Membrane Potential Detection Kit (JC-1) (C2003S), Crystal violet (Y268091-100g), and ATP Detection Kit (S0026) were purchased from Shanghai Beyotime Biotechnology Co., Ltd. ABTS Free Radical Scavenging Capacity Detection Kit (BC4770) and Alamar Blue Cell Viability Assay Reagent (A7631) were purchased from Beijing Solarbio Science & Technology Co., Ltd. Reduced glutathione (GSH) assay kit (A006-2-1), superoxide dismutase (SOD) typed assay kit (A001-2-2), and microscale malondialdehyde (MDA) assay kit (A003-2-2) were purchased from Nanjing Jiancheng Bioengineering Institute. Matrigel (CLS354277) was purchased from Merck Chemical Technology (Shanghai) Co., Ltd. TNF-α (A11534), IL-6 (A11115), IL-1β (A27676), IL-10 (A15680), TGF-β (A25313), Arg-1 (A25808), VEGF (A23759), CD31 (A19014), FOXO3A (A17978), p21 (A22460), AMPK alpha (A27740), Phospho-AMPKα1 (AP1441), PGC1α (A11971), and SIRT1 (A17307) were purchased from Abcepta Biotechnology Co., Ltd. ATP5A1 (DF3806) and COX42 (AF0663) were purchased from Affinity Biosciences. All PCR primers were designed and synthesized by Shanghai Sangon Biotech Co., Ltd. HUVECs, mouse macrophages (RAW264.7 cells), and L929 cells were all purchased from the Cell Bank of the Chinese Academy of Sciences, Shanghai.

4.2 Synthesis of PDA@RES NPs and HAMA hydrogel

First, 8.4 mL of Tris buffer at pH 8.5 was placed in a glass vial, followed by addition of 1 mL anhydrous ethanol and 1.6 mL dopamine hydrochloride solution (30 mM). The mixture was stirred at 50 °C for 3 h to synthesize polydopamine nanoparticles. Subsequently, the system was adjusted to 12 mL by sequentially adding 1 mL anhydrous ethanol, 100 μL formaldehyde, 100 μL ammonia water, and 1000 μL resveratrol solution (20 mg resveratrol dissolved in 1 mL anhydrous ethanol). The mixture was stirred at room temperature for 1 h to synthesize PDA@RES NPs.

HAMA was synthesized according to the method described in the literature [76]. Briefly, 1 gram of HA was dissolved in 100 mL of water with stirring until completely dissolved. The solution was then placed in an ice bath, and 1 mL of methacrylic anhydride was added to initiate the reaction. During the reaction, the pH was maintained at 8–8.5, and the reaction was continued for 12 h. After the reaction, the solution was dialyzed against water for 2 days and then lyophilized to obtain the HAMA product. Subsequently, the HAMA product was prepared into a 5% (w/v) pre-gel solution containing photoinitiator LAP. The synthesized PDA@RES nanoparticles were then uniformly dispersed into this solution. Finally, the mixture was crosslinked by UV light irradiation to obtain the PDA@RES-loaded composite hydrogel.

4.3 Characterization of PDA@RES NPs

The morphological characteristics of PDA@RES NPs were observed using TEM (Talos F200S microscope; SUPER X energy-dispersive spectroscopy). Their particle size distribution and Zeta potential were measured using DLS (Malvern Zetasizer Nano ZS nanoparticle size analyzer). Their optical properties were analyzed using ultraviolet–visible spectrophotometry (UV–vis, UV 3600I plus). The elemental composition and chemical state of the sample surface were analyzed using XPS (Thermo Fisher K-ALPHA). Their functional groups were determined using FTIR (Thermo Fisher Nicolet Is5), and their thermal stability was evaluated using TGA (Hitachi STA200/Hitachi STA300). The photothermal conversion capabilities of PDA NPs and PDA@RES NPs were compared by irradiation with an 808 nm NIR laser for 6 min, and temperature changes were recorded using an infrared thermal imager. Subsequently, the effects of different concentrations of PDA@RES NPs and different powers of NIR laser on the photothermal conversion efficiency of the nanosystem were further explored. Finally, the photothermal cycling stability and reproducibility of PDA@RES NPs were evaluated by performing 5

heating and cooling cycles under NIR irradiation.

4.4 Drug loading and *in vitro* release study

The DLC and EE of PDA@RES were determined using UV–vis spectrophotometry. Briefly, the supernatant was collected after centrifugation during the synthesis process, and the concentration of unloaded RES was measured at 306 nm based on a pre-established standard calibration curve. The DLC and EE were calculated using the following equations (Eqs. (1) and (2)):

$$\mathrm{EE}\,(\%) = \frac{W_{\mathrm{total}} - W_{\mathrm{free}}}{W_{\mathrm{total}}} \times 100\% \quad (1)$$

$$\mathrm{DLC}\,(\%) = \frac{W_{\mathrm{total}} - W_{\mathrm{free}}}{W_{\mathrm{PDA}} + W_{\mathrm{total}} - W_{\mathrm{free}}} \times 100\% \quad (2)$$

where W_{total} represents the total weight of RES added, W_{free} is the weight of unloaded RES in the supernatant, and W_{PDA} is the initial weight of PDA nanoparticles. For the *in vitro* release assessment, PDA@RES dispersions were sealed in dialysis bags and immersed in PBS buffered at pH 7.4 or 5.5 to simulate physiological and wound microenvironments, respectively. The system was maintained at 37 °C with constant shaking. To evaluate the NIR-responsive release, specific groups were exposed to an 808 nm laser (1.5 W/cm^2) for 5 min at predetermined time points (6, 12, 18, 24, 30, 36, 42 and 48 h). At scheduled intervals, 1 mL of the release medium was withdrawn for quantification and immediately replaced with an equal volume of fresh buffer.

4.5 Cell culture

This study used L929 cells, HUVECs, and RAW264.7 cells for *in vitro* experiments. L929 cells were cultured in Dulbecco's modified Eagle medium (DMEM) supplemented with 10% fetal bovine serum, 100 U/mL Penicillin, and 100 U/mL Streptomycin. HUVECs were cultured in endothelial cell-specific culture medium (ECM). RAW 264.7 cells were cultured in DMEM supplemented with 10% fetal bovine serum. All cells were cultured at 37 °C in an incubator containing 5% carbon dioxide.

4.6 Biocompatibility assessment

To evaluate the biocompatibility of PDA@RES NPs, L929 cells were seeded in 96-well plates and cultured in fresh medium containing different concentrations of PDA@RES NPs for 1, 2, and 3 days, with groups set up with or without near-infrared light irradiation. Cell viability was detected using the CCK-8 reagent kit by measuring OD values at 450 nm. Meanwhile, after 24 h of co-culture, cells were stained with the Calcein-AM/PI live/dead cell staining kit, and cell survival status was observed under a fluorescence microscope. *In vivo* safety was evaluated through histological sections of animal heart, liver, spleen, lung, and kidney organs.

4.7 *In vitro* evaluation of antioxidant and anti-inflammatory capabilities of PDA@RES NPs

The *in vitro* antioxidant capacity of PDA@RES NPs was evaluated using the ABTS free radical scavenging assay kit. RAW264.7 cells were induced with LPS (1 μg/mL) for 4 h, then the medium was replaced with medium containing different treatment groups and cultured for an additional 24 h. Reduced glutathione content, superoxide dismutase activity, and malondialdehyde content as a lipid peroxidation end-product were analyzed using assay kits. Intracellular ROS were analyzed under a microscope using the 2',7'-dichlorodihydrofluorescein diacetate (DCFH-DA) probe. In the anti-inflammatory assessment, the actual expression of M1-type markers TNF-α, IL-6, and IL-1β, as well as M2-type markers IL-10, TGF-β, and Arg-1, was detected by qRT-PCR and immunofluorescence staining. Immunofluorescence procedure: After discarding the culture medium, cells were fixed with paraformaldehyde for 15 min, then washed with PBS 3 times, 5 min each. Cells were blocked with immunofluorescence staining blocking solution for 1 h. After primary antibody incubation overnight at 4 °C, the primary antibody was recovered. Subsequently, cells were washed with PBS 3 times, 5 min each. Secondary antibody was incubated at room temperature for 1 h and then recovered. Cells were washed with PBS 3 times, 5 min each. 4',6-diamidino-2-phenylindole (DAPI) was incubated for 5 min and then recovered. Cells were washed with PBS 3 times, 5 min each, and observed under a laser scanning confocal microscope. After transcriptomic analysis, validation was performed through ATP production, NADH/NAD$^+$ ratio, mitochondrial ROS staining, transmission electron microscopy analysis of mitochondrial morphology, MitoTracker Green/MitoTracker Red CMXRos mitochondrial staining, qRT-PCR, Western blot, and immunofluorescence.

4.8 *In vitro* evaluation of angiogenic capacity of PDA@RES NPs

HUVECs were used for pro-angiogenic capacity assessment. First, cell migration capacity was evaluated through scratch assays. After HUVECs reached confluence, scratches were made and photographed at 0, 24, and 36 h to calculate the scratch healing rate. Vertical migration was analyzed using Transwell chambers. After 6 h, crystal violet staining was performed for microscopic analysis. Finally, Matrigel tube formation assays were conducted. HUVECs were seeded on pre-coated Matrigel and treated with different groups. After 6–8 h of culture, tube formation was observed, and branch points and total tube length were quantitatively analyzed. Angiogenesis-related genes and proteins were detected by qRT-PCR and immunofluorescence staining.

4.9 *In vivo* animal experiments

All animals were treated according to the ethical principles of laboratory animal welfare (CKARI202315) and followed the guidelines of the Animal Care and Use Committee. Thirty-six male Sprague-Dawley rats weighing approximately 250 grams were selected. After fasting for 12 h, rats were intraperitoneally injected with 1% Streptozotocin. Seven days later, blood glucose was randomly collected from the tail vein. When the randomly measured blood glucose value exceeded 16.7 mmol/L, the diabetes model was considered successfully established. To establish a chronic wound animal model, rats were anesthetized, then all hair on the dorsal skin was shaved, and a circular full-thickness skin defect wound with a diameter of approximately 15 mm was created on the back of each rat. All rats were randomly divided into four groups: Control group, HAMA group, HAPR group, and HAPRN group. Wounds were photographed on days 0, 3, 7, 10, and 14. Images acquired were analyzed using ImageJ software. Wound healing rates of different groups were calculated according to the formula. Rats were sacrificed on days 7 and 14, and wound tissues were collected for paraffin embedding and sectioning. Inflammation and tissue morphology were assessed by H&E

staining, collagen deposition was assessed by Masson's trichrome staining, and neovascular density and inflammatory microenvironment were assessed by immunofluorescence staining of CD31, α-SMA, iNOS, and CD206.

4.10 Statistical analysis

All acquired data were processed using GraphPad Prism v8.0. Student's t-test was used for comparison between two groups, while analysis of variance (ANOVA) model was employed for comparison among multiple groups. The data are presented as mean ± standard error of the mean of the measured values (*P < 0.05, **P < 0.01, ***P < 0.001, ****P < 0.0001).

Electronic Supplementary Material: Supplementary material (including additional figures demonstrating material characterizations, *in vitro* and *in vivo* biocompatibility assays, bio-TEM observations, qRT-PCR primer sequences, and detailed calculations of the photothermal conversion efficiency) is available in the online version of this article at https://doi.org/10.26599/NR.2026.94908573.

Data availability

All data needed to evaluate the conclusions in the paper are present in the paper and the Supplementary Materials.

Acknowledgements

This work was funded by the National Nature Science Foundation of China (Nos. 82371006 and 82501102); the Science and Technology Projects of the Finance Department of Jilin Province (No. jcsz2025678-3); the China Postdoctoral Science Foundation (No. 2025M771755); the Postdoctoral Fellowship Program (Grade C) of China Postdoctoral Science Foundation (No. GZC20251217).

Declaration of competing interest

The authors declare no conflicts of interest.

Author contribution statement

J. F.: Conceptualization, methodology, data curation, investigation, writing – original draft. H. X. L.: Writing – original draft, data curation, investigation. S. C. R. and Y. M. Z.: Conceptualization, methodology. Y. Z. H. and M. C. L.: Data curation, investigation. J. X. C., J. X. L., and D. X. H.: Investigation, visualization. Y. D. Z.: Supervision, project administration, writing – review & editing. Y. M. Z.: Conceptualization, supervision, funding acquisition, project administration, resources, writing – review & editing.

Informed consent

Not applicable.

Ethics statement

All animal experiments were reviewed and approved by the Animal Care and Use Committee of Jilin University (No. CKARI202315).

Use of AI statement

None.

References

[1] Wang, R. Y.; Gu, S.; Kim, Y. H.; Lee, A.; Lin, H. D.; Jiang, D. S. Diabetic wound repair: From mechanism to therapeutic opportunities. *MedComm* **2025**, *6*, e70406.
[2] Wang, X. X.; Song, X. R.; Feng, W.; Chang, M. Q.; Yang, J. S.; Chen, Y. Advanced nanomedicines for treating refractory inflammation-related diseases. *Nano-Micro Lett.* **2025**, *17*, 323.
[3] Zhou, Q. L.; Zhuang, Y.; Deng, X. L.; Jiang, W. D.; Wang, X. D.; Yuan, C. Y.; Lin, K. L. Hydrogel-based ROS-regulating strategy: Reprogramming the oxidative stress imbalance in advanced diabetic wound repair. *Adv. Mater.* **2026**, *38*, e12719.
[4] Yuan, P. Y.; Deng, M.; Li, X. R.; Lu, X. T.; Yang, H.; Jin, R. H.; Wang, L.; Chen, M.; Bai, T.; Liu, T. et al. *Lactobacillus* extracellular vesicle-driven oxygen-releasing photothermal hydrogel reprograms macrophages and promotes angiogenesis to accelerate diabetic wound healing. *Bioact. Mater.* **2025**, *54*, 144–158.
[5] Ding, K. X.; Zhang, Z. P.; Han, Z. B.; Shi, L.; Li, X. Z.; Liu, Y. T.; Li, Z. Z.; Zhao, C. C.; Cui, Y. F.; Zhou, L. Y. et al. Liver ALKBH5 regulates glucose and lipid homeostasis independently through GCGR and mTORC1 signaling. *Science* **2025**, *387*, eadp4120.
[6] Feng, J.; Chen, Z. W.; Ma, Y. Q.; Yang, X. Y.; Zhu, Z. J.; Zhang, Z. W.; Hu, J. J.; Liang, W.; Ding, G. H. AKAP1 contributes to impaired mtDNA replication and mitochondrial dysfunction in podocytes of diabetic kidney disease. *Int. J. Biol. Sci.* **2022**, *18*, 4026–4042.
[7] Willenborg, S.; Sanin, D. E.; Jais, A.; Ding, X. L.; Ulas, T.; Nüchel, J.; Popović, M.; MacVicar, T.; Langer, T.; Schultze, J. L. et al. Mitochondrial metabolism coordinates stage-specific repair processes in macrophages during wound healing. *Cell Metab.* **2021**, *33*, 2398–2414.e9.
[8] Xu, Z. Y.; Yang, Y.; Li, X. H.; Wang, J.; Chen, S. D.; An, T. T.; Hu, C.; Deng, C.; Zhou, F.; Xiang, L. et al. A visible-light photocatalysis/hydrolysis hydrogen-generating nanoplatform for dynamic inflammation management via immune metabolism orchestration during wound repair. *ACS Appl. Mater. Interfaces* **2025**, *17*, 24918–24939.
[9] Pang, B. X.; Dong, G. T.; Pang, T. L.; Sun, X. Y.; Liu, X.; Nie, Y. F.; Chang, X. Emerging insights into the pathogenesis and therapeutic strategies for vascular endothelial injury-associated diseases: Focus on mitochondrial dysfunction. *Angiogenesis* **2024**, *27*, 623–639.
[10] Kawaguchi, S. I.; Sato, K.; Izawa, J.; Takayama, N.; Hayakawa, H.; Tominaga, K.; Endo, H.; Kouki, T.; Ohno, N.; Kanda, Y. The combination of venetoclax with dimethyl fumarate synergistically induces apoptosis in AML cells by disrupting mitochondrial integrity through ROS accumulation. *Cell Death Dis.* **2025**, *16*, 750.
[11] Yang, Y. Q.; Chen, Q. H.; Ying, X. H.; Wu, Z. Y.; Zeng, W.; Miao, C. X.; Nan, Y. Y.; Huang, Q.; Ai, K. L. Fully biocompatible tantalum-based antioxidant nanoshields for proximal tubule epithelial cells-targeted mitochondrial holistic protection in acute kidney injury. *Adv. Mater.* **2026**, *38*, e06307.
[12] Liu, T. T.; Kong, X. R.; Qiao, J. B.; Wei, J. S. Decoding Parkinson's disease: The interplay of cell death pathways, oxidative stress, and therapeutic innovations. *Redox Biol* **2025**, *85*, 103787.
[13] Yao, H.; He, Q. M.; Wei, S. J.; Xiang, L.; Luo, Y. Y.; Huang, C.; Liu, W. W.; Zheng, C.; Li, X. P.; Gao, Y. X. Targeted inhibition of macrophage STING signaling alleviates inflammatory injury and ventricular remodeling in acute myocardial infarction. *Acta Pharm. Sin. B* **2025**, *15*, 4030–4046.
[14] Wang, Q.; Zhang, M. Y.; Jiang, W. H.; Li, D. J.; Qi, B. J.; Shi, S.; Shi, S.; Yi, C. Q. Spontaneous hydrogen-releasing nanoenzyme alleviates osteoarthritis via oxidative stress reduction and mitochondrial dysfunction reversal. *J. Nanobiotechnol.* **2025**, *23*, 662.
[15] Yao, R. Q.; Ren, C.; Xia, Z. F.; Yao, Y. M. Organelle-specific autophagy in inflammatory diseases: A potential therapeutic target underlying the quality control of multiple organelles. *Autophagy* **2021**, *17*, 385–401.
[16] Cai, L.; Swetha, M.; Raji, A.; Terry, A. V. Jr.; Raju, R. P. Mitochondria-targeted therapy with metformin and MitoQ reduces

oxidative stress, improves mitochondrial function, and restores metabolic homeostasis in a murine model of Gulf War Illness. *Redox Biol*. **2025**, *85*, 103714.
[17] Skawratananond, S.; Xiong, D. X.; Zhang, C.; Tonk, S.; Pinili, A.; Delacruz, B.; Pham, P.; Smith, S. C.; Navab, R.; Reddy, P. H. Mitophagy in Alzheimer's disease and other metabolic disorders: A focus on mitochondrial-targeted therapeutics. *Ageing Res. Rev.* **2025**, *108*, 102732.
[18] Picca, A.; Faitg, J.; Auwerx, J.; Ferrucci, L.; D'Amico, D. Mitophagy in human health, ageing and disease. *Nat. Metab.* **2023**, *5*, 2047–2061.
[19] Yao, W. D.; Zhou, J. N.; Tang, C.; Zhang, J. L.; Chen, Z. Y.; Li, Y.; Gong, X. J.; Qu, M. Y.; Zeng, Q.; Jia, Y. L. et al. Hydrogel microneedle patches loaded with stem cell mitochondria-enriched microvesicles boost the chronic wound healing. *ACS Nano* **2024**, *18*, 26733–26750.
[20] Rabie, M. A.; Madry, H.; Cucchiarini, M.; El-Sayed, N. S. The brain-joint axis: Links between osteoarthritis and neurodegenerative disorders in aging. *J. Adv. Res*., in press, DOI: 10.1016/j.jare.2025.10.023.
[21] Roussos, A.; Kitopoulou, K.; Borbolis, F.; Ploumi, C.; Gianniou, D. D.; Li, Z. Q.; He, H. J.; Tsakiri, E.; Borland, H.; Kostakis, I. K. et al. Urolithin A modulates inter-organellar communication via calcium-dependent mitophagy to promote healthy ageing. *Autophagy* **2025**, *21*, 3097–3122.
[22] Chen, L. Y.; Fan, Y. J.; Jiang, N.; Huang, X. S.; Yu, M.; Zhang, H.; Xu, Z. R.; He, D. D.; Wang, Y.; Ding, C. Y. et al. An energy metabolism-engaged nanomedicine maintains mitochondrial homeostasis to alleviate cellular ageing. *Nat. Nanotechnol.* **2025**, *20*, 1332–1344.
[23] Liu, Y.; Li, Y. T.; Yin, Y.; Yu, L.; Ma, H. Micro/nanoplastic-driven cardiovascular senescence and multi-target intervention by traditional Chinese medicine. *Ageing Res. Rev.* **2025**, *111*, 102841.
[24] Mazan-Mamczarz, K.; Tsitsipatis, D.; Childs, B. G.; Carr, A. E.; Dos Santos, C. R.; Anerillas, C.; Romero, B.; Gregg, J. M.; Henry-Smith, C.; Okereke, A. N. et al. Single-cell and spatial transcriptomics map senescent vascular cells in arterial remodeling during atherosclerosis in mice. *Nat. Aging* **2025**, *5*, 1528–1547.
[25] Yang, H.; Chen, Y. F.; Rong, Y. C.; Zhou, Y. X.; Li, S. T.; Li, X. H.; Wu, H. L.; Lv, D. M.; Cao, X. L.; Wang, P. et al. Multifunctional hydrogel targeting senescence to accelerate diabetic wound healing through promoting angiogenesis. *J. Nanobiotechnol.* **2025**, *23*, 177.
[26] Jiang, S. L.; Wang, D.; Zou, C.; Zhu, Z. W.; Luo, C.; Wang, Z. B. Macrophages at the crossroads of cellular senescence and cancer development and progression: Therapeutic opportunities and challenges. *Pharmacol. Ther.* **2025**, *274*, 108906.
[27] Zhang, Q.; Zhang, C. L.; Kang, C. J.; Zhu, J. R.; He, Q. S.; Li, H. W.; Tong, Q.; Wang, M.; Zhang, L. L.; Xiong, X. et al. Liraglutide promotes diabetic wound healing via Myo1c/Dock5. *Adv. Sci.* **2024**, *11*, 2405987.
[28] Zhong, W. J.; Wang, X. Y.; Yang, L. X.; Wang, Y.; Xiao, Q. Y.; Yu, S. M.; Cannon, R. D.; Bai, Y.; Zhang, C. W.; Chen, D. J. et al. Nanocarrier-assisted delivery of metformin boosts remodeling of diabetic periodontal tissue via cellular exocytosis-mediated regulation of endoplasmic reticulum homeostasis. *ACS Nano* **2022**, *16*, 19096–19113.
[29] Xu, P.; Zhou, W.; Wang, S. D.; Wang, L. J.; Bai, Y.; Xing, S.; Xue, W. D.; Li, M.; Shi, J.; Wu, H. X. Alisol A ameliorates vascular cognitive impairment via AMPK/NAMPT/SIRT1-mediated regulation of cholesterol and autophagy. *Theranostics* **2025**, *15*, 9415–9446.
[30] Packer, M. Intensity, duration, and context dependency of the responses to nutrient surplus and deprivation signaling in the heart: Insights into the complexities of cardioprotection. *Circulation* **2025**, *152*, 802–835.
[31] Malik, N.; Shaw, R. J. The AMPK pathway: Molecular rejuvenation of metabolism and mitochondria. *Annu. Rev. Cell Dev. Biol.* **2025**, *41*, 375–402.
[32] Varga, K.; Sikur, N.; Paszternák, A.; Friesenhahn, A. L.; Zymela, F. E.; Bagaméry, F.; Tábi, T.; Wölfl, S. Resveratrol restores insulin signaling and balances mitochondrial biogenesis and autophagy in streptozotocin-induced neurodegeneration *in vitro*. *Eur. J. Pharm. Sci.* **2025**, *212*, 107202.
[33] Ungurianu, A.; Zanfirescu, A.; Margină, D. Sirtuins, resveratrol and the intertwining cellular pathways connecting them. *Ageing Res. Rev.* **2023**, *88*, 101936.
[34] Zhang, T.; Chi, Y. Q.; Kang, Y. L.; Lu, H.; Niu, H. L.; Liu, W.; Li, Y. Resveratrol ameliorates podocyte damage in diabetic mice via SIRT1/PGC-1α mediated attenuation of mitochondrial oxidative stress. *J. Cell. Physiol.* **2019**, *234*, 5033–5043.
[35] Chen, Y. Y.; Zhang, C.; McClements, D. J.; Zhou, Y. Y.; Yin, X. G.; Shen, R. P.; Tang, X.; Zhu, K. W.; Luo, X. Replacing OSA starch: A novel maltodextrin-vitamin E succinate conjugate with superior emulsifying and antioxidant performance in resveratrol-loaded nanoemulsions. *Carbohydr. Polym.* **2025**, *370*, 124445.
[36] Huangfu, H.; Du, S. L.; Zhang, H.; Wang, H. C.; Zhang, Y.; Yang, Z.; Zhang, X. W.; Ren, S. C.; Chen, S. Y.; Wang, C. Z. et al. Facile engineering of resveratrol nanoparticles loaded with 20(S)-protopanaxadiol for the treatment of periodontitis by regulating the macrophage phenotype. *Nanoscale* **2023**, *15*, 7894–7908.
[37] Kong, J. L.; Ma, S. H.; Chu, R. X.; Liu, J. W.; Yu, H. R.; Mao, M. R.; Ge, X. H.; Sun, Y. T.; Wang, Y. Photothermal and photocatalytic glycol chitosan and polydopamine-grafted oxygen vacancy bismuth oxyiodide ($BiO_{1-x}I$) nanoparticles for the diagnosis and targeted therapy of diabetic wounds. *Adv. Mater.* **2024**, *36*, 2307695.
[38] Wang, Y.; Zhao, W. N.; Lee, Y.; Li, Y. N.; Wang, Z. K.; Tam, K. C. Thermo-adaptive interfacial solar evaporation enhanced by dynamic water gating. *Nat. Commun.* **2024**, *15*, 6157.
[39] Xie, H. H.; Yang, M.; He, X. L.; Zhan, Z.; Jiang, H. D.; Ma, Y. M.; Hu, C. Z. Polydopamine-modified 2D Iron (II) immobilized $MnPS_3$ nanosheets for multimodal imaging-guided cancer synergistic photothermal-chemodynamic therapy. *Adv. Sci.* **2024**, *11*, 2306494.
[40] Zhao, Y.; Wang, W. K.; Liu, M. Y.; Cai, Y. F.; Wang, Y. F.; Dong, Y.; Bai, Y. K.; Zhu, J. F.; Tay, F. R.; Niu, L. N. Mn_3O_4-potentiated bifunctional hydrogel for mild temperature-controlled tumor ablation and osteogenesis. *Bioact. Mater.* **2026**, *55*, 391–409.
[41] Ma, L. L.; Zhou, Y. L.; Zhang, Z. W. B.; Liu, Y. Q.; Zhai, D.; Zhuang, H.; Li, Q.; Yuye, J.; Wu, C. T.; Chang, J. Multifunctional bioactive Nd–Ca–Si glasses for fluorescence thermometry, photothermal therapy, and burn tissue repair. *Sci. Adv.* **2020**, *6*, eabb1311.
[42] Wu, G. L.; Tan, S. Y.; Wu, F.; Xiao, H.; Zhao, B. B.; Li, C. Q.; Zhen, J. K.; Tang, X.; Yang, Q. L.; Chen, G. D. Rational design of ultrabright NIR-II nanofluorophores with enhanced photothermal conversion efficiency for targeted chemodynamic-hypothermal photothermal therapy of hepatocellular carcinoma. *Mater. Today Bio* **2025**, *35*, 102362.
[43] Yang, A. P.; Sun, Y. N.; Lyu, B.; Chen, B. L.; Fan, Z. P.; Li, M. H.; Zhao, Y.; Fu, J. J.; He, B.; Zhang, H. et al. One-pot preparation of nanodispersion with readily available components for localized tumor photothermal and photodynamic therapy. *Asian J. Pharm. Sci.* **2022**, *17*, 120–128.
[44] Xiao, Z. P.; Zhou, J. L.; Chen, H. Q.; Chen, X.; Wang, L.; Liu, D. B.; Kang, X. C. Synthesis, characterization and MAFLD prevention potential of Ganoderma lucidum spore polysaccharide-stabilized selenium nanoparticles. *Int. J. Biol. Macromol.* **2024**, *282*, 136962.
[45] Guan, X. Q.; Wang, Y. C.; Yu, W. K.; Wei, Y.; Lu, Y.; Dai, E. Y.; Dong, X. W.; Zhao, B.; Hu, C.; Yuan, L. et al. Blocking ubiquitin-specific protease 7 induces ferroptosis in gastric cancer via targeting stearoyl-CoA desaturase. *Adv. Sci.* **2024**, *11*, 2307899.
[46] Levi-D'Ancona, E.; Stendahl, A. M.; Henry-Kanarek, B. A.; Davidson, R. K.; Walker, E. M.; Soleimanpour, S. A. Mitophagy in the adaptation to pancreatic β cell stress in diabetes. *Trends Endocrinol. Metab*., in press, DOI: 10.1016/j.tem.2025.09.009.
[47] Li, M. H.; Yang, Q. W.; Gao, J.; Liu, X. D.; Shi, J. H.; Guo, W. Z.; Zhang, Y.; Yu, Q. W.; Sun, X. Z.; Zhang, S. J. Nanotuner targeting mitochondrial redox and iron homeostasis imbalance for the treatment of acute liver injury. *Theranostics* **2025**, *15*, 9131–9158.
[48] Yang, L.; Wei, X.; Liao, Z.; Chen, B.; Zeng, G.; Mei, Z. G. Role of

mitochondria transmission in ischemic stroke: Friend or foe. *Redox Biol.* **2025**, *87*, 103868.
[49] Shao, H. W.; Xu, S. X.; Zeng, F. C.; Jin, Z. Y.; Ji, X. F.; Shan, Z. M.; Kang, J. L.; Tian, Q. Y.; Zhang, S. A.; Mao, Z. N. et al. Metal-organic framework-integrated nanoplatform orchestrates osteochondral-synovial homeostasis for osteoarthritis therapy. *ACS Nano* **2025**, *19*, 32744–32766.
[50] Liu, X. Y.; Tian, H. Y.; Wang, D. Y.; Nie, F. J.; Chen, Y.; Wang, Y.; Zhang, L. G.; Li, J. H.; Wu, J. L. Ligand-metal charge transfer-enabled copper-gallate nanozyme rescue oxidative stressed reparative cells for inflammatory dental tissue regeneration. *Biomaterials* **2026**, *326*, 123672.
[51] Yang, X.; Rong, K. W.; Fu, S. T.; Yang, Y. Z.; Liu, S. S.; Zhang, C. Y.; Xu, K.; Zhang, K.; Zhu, Y. C.; Hao, Y. Q. et al. Engineered *Spirulina platensis* for treating rheumatoid arthritis and restoring bone homeostasis. *Nat. Commun.* **2025**, *16*, 4434.
[52] Cui, Y. X.; Chen, J. H.; Zhang, Z.; Shi, H. Y.; Sun, W. C.; Yi, Q. The role of AMPK in macrophage metabolism, function and polarisation. *J. Transl. Med.* **2023**, *21*, 892.
[53] Jin, Z. Z.; Chang, B. H.; Wei, Y. L.; Yang, Y.; Zhang, H.; Liu, J. B.; Piao, L.; Bai, L. H. Curcumin exerts chondroprotective effects against osteoarthritis by promoting AMPK/PINK1/Parkin-mediated mitophagy. *Biomed. Pharmacother.* **2022**, *151*, 113092.
[54] Zhuge, A. X.; Li, S. J.; Han, S. Y.; Yuan, Y.; Shen, J.; Wu, W. R.; Wang, K. C.; Xia, J. F.; Wang, Q. Q.; Gu, Y. F. et al. Akkermansia muciniphila-derived acetate activates the hepatic AMPK/SIRT1/PGC-1α axis to alleviate ferroptosis in metabolic-associated fatty liver disease. *Acta Pharm. Sin. B* **2025**, *15*, 151–167.
[55] Barcena, M. L.; Tonini, G.; Haritonow, N.; Breiter, P.; Milting, H.; Baczko, I.; Müller-Werdan, U.; Ladilov, Y.; Regitz-Zagrosek, V. Sex and age differences in AMPK phosphorylation, mitochondrial homeostasis, and inflammation in hearts from inflammatory cardiomyopathy patients. *Aging Cell* **2023**, *22*, e13894.
[56] Zhang, L. L.; Xin, C. H.; Wang, S.; Zhuo, S. X.; Zhu, J.; Li, Z.; Liu, Y. Y.; Yang, L. F.; Chen, Y. Lactate transported by MCT1 plays an active role in promoting mitochondrial biogenesis and enhancing TCA flux in skeletal muscle. *Sci. Adv.* **2024**, *10*, eadn4508.
[57] Liu, H.; Zhen, C. E.; Xie, J. M.; Luo, Z. H.; Zeng, L.; Zhao, G. J.; Lu, S. H.; Zhuang, H. X.; Fan, H. L.; Li, X. et al. TFAM is an autophagy receptor that limits inflammation by binding to cytoplasmic mitochondrial DNA. *Nat. Cell Biol.* **2024**, *26*, 878–891.
[58] Liu, R. X.; Li, F. J.; Hao, S.; Hou, D. Y.; Zeng, X.; Huang, H.; Sethi, G.; Guo, J.; Duan, C. Y. Low-dose Olaparib improves septic cardiac function by reducing ferroptosis via accelerated mitophagy flux. *Pharmacol. Res.* **2024**, *200*, 107056.
[59] Yu, B.; Ma, J.; Li, J.; Wang, D. Z.; Wang, Z. G.; Wang, S. S. Mitochondrial phosphatase PGAM5 modulates cellular senescence by regulating mitochondrial dynamics. *Nat. Commun.* **2020**, *11*, 2549.
[60] Riegger, J.; Schoppa, A.; Ruths, L.; Haffner-Luntzer, M.; Ignatius, A. Oxidative stress as a key modulator of cell fate decision in osteoarthritis and osteoporosis: A narrative review. *Cell. Mol. Biol. Lett.* **2023**, *28*, 76.
[61] Liu, Y.; Ao, X.; Ding, W.; Ponnusamy, M.; Wu, W.; Hao, X. D.; Yu, W. P.; Wang, Y. F.; Li, P. F.; Wang, J. X. Critical role of FOXO3a in carcinogenesis. *Mol. Cancer* **2018**, *17*, 104.
[62] Wang, B. S.; Han, J.; Elisseeff, J. H.; Demaria, M. The senescence-associated secretory phenotype and its physiological and pathological implications. *Nat. Rev. Mol. Cell Biol.* **2024**, *25*, 958–978.
[63] Zhang, J.; Luo, Q.; Hu, Q.; Zhang, T. T.; Shi, J. Y.; Kong, L.; Fu, D. H.; Yang, C. L.; Zhang, Z. P. An injectable bioactive dressing based on platelet-rich plasma and nanoclay: Sustained release of deferoxamine to accelerate chronic wound healing. *Acta Pharm. Sin. B* **2023**, *13*, 4318–4336.
[64] Zhang, S. F.; Gatsi, B.; Yao, X.; Jin, Y.; Amhal, H. Cellulose nanofiber-reinforced antimicrobial and antioxidant multifunctional hydrogel with self-healing, adhesion for enhanced wound healing. *Carbohydr. Polym.* **2025**, *352*, 123189.
[65] Yu, P. C.; Wilhelm, K.; Dubrac, A.; Tung, J. K.; Alves, T. C.; Fang, J. S.; Xie, Y.; Zhu, J.; Chen, Z. H.; De Smet, F. et al. FGF-dependent metabolic control of vascular development. *Nature* **2017**, *545*, 224–228.
[66] Mottet, D.; Bellahcene, A.; Pirotte, S.; Waltregny, D.; Deroanne, C.; Lamour, V.; Lidereau, R.; Castronovo, V. Histone deacetylase 7 silencing alters endothelial cell migration, a key step in angiogenesis. *Circ. Res.* **2007**, *101*, 1237–1246.
[67] Paddock, C.; Zhou, D. W.; Lertkiatmongkol, P.; Newman, P. J.; Zhu, J. Q. Structural basis for PECAM-1 homophilic binding. *Blood* **2016**, *127*, 1052–1061.
[68] Gamble, J. R.; Drew, J.; Trezise, L.; Underwood, A.; Parsons, M.; Kasminkas, L.; Rudge, J.; Yancopoulos, G.; Vadas, M. A. Angiopoietin-1 is an antipermeability and anti-inflammatory agent *in vitro* and targets cell junctions. *Circ. Res.* **2000**, *87*, 603–607.
[69] Schuurmans, C. C. L.; Mihajlovic, M.; Hiemstra, C.; Ito, K.; Hennink, W. E.; Vermonden, T. Hyaluronic acid and chondroitin sulfate (meth)acrylate-based hydrogels for tissue engineering: Synthesis, characteristics and pre-clinical evaluation. *Biomaterials* **2021**, *268*, 120602.
[70] Andolfi, A.; Cai, L.; González Martínez, M. V.; Garciamendez-Mijares, C. E.; Del Valle Rodríguez, F.; Garza Garza, R.; Kuai, A. R.; Kuang, X.; Nejjari, J.; Zhang, Y. S. Hyaluronic acid-based bioink for anisotropic neural tissue cryobioprinting. *Int. J. Extrem. Manuf.* **2026**, *8*, 015003.
[71] Liu, H. Z.; Wang, F.; Yi, W. W.; Huang, S. Y.; Tang, Z. X.; Liao, B.; Hu, Z. M.; Cui, W. G.; Shen, J. L. Internal-friction network piezoelectric hydrogel microspheres achieve physiological electrical adaptation to regulate mitochondrial autophagy in degenerative tissues. *Adv. Mater.* **2026**, *38*, e19152.
[72] Xiong, M. C.; Yang, X. L.; Shi, Z. W.; Xiang, J. B.; Gao, H. H.; Ji, S. F.; Li, Y. Y.; Pi, W.; Chen, H. T.; Zhang, H. L. et al. Programmable artificial skins accomplish antiscar healing with multiple appendage regeneration. *Adv. Mater.* **2024**, *36*, 2407322.
[73] Yang, Y.; Chu, C. Y.; Liu, L.; Wang, C. B.; Hu, C.; Rung, S.; Man, Y.; Qu, Y. L. Tracing immune cells around biomaterials with spatial anchors during large-scale wound regeneration. *Nat. Commun.* **2023**, *14*, 5995.
[74] Wang, Y. Z.; Yuan, X. Y.; Yao, B.; Zhu, S. J.; Zhu, P.; Huang, S. Tailoring bioinks of extrusion-based bioprinting for cutaneous wound healing. *Bioact. Mater.* **2022**, *17*, 178–194.
[75] An, T. T.; Xu, Z. Y.; Yang, Y.; Li, X. H.; Chen, S. D.; Yang, X. M.; Man, Y.; Hu, C.; Qu, Y. L. EGCG-releasing nanofibrous scaffold enhances wound healing via γδ T cells modulation. *Biomaterials* **2026**, *325*, 123543.
[76] Chen, J. Q.; Yang, J. B.; Wang, L.; Zhang, X. W.; Heng, B. C.; Wang, D. A.; Ge, Z. G. Modified hyaluronic acid hydrogels with chemical groups that facilitate adhesion to host tissues enhance cartilage regeneration. *Bioact. Mater.* **2021**, *6*, 1689–1698.